Journal of Computational Physics 313 (2016) 635–653

Contents lists available at ScienceDirect

Journal of Computational Physics

www.elsevier.com/locate/jcp

A nonlinear manifold-based reduced order model for multiscale analysis of heterogeneous hyperelastic materials

Satyaki Bhattacharjee, Karel Matouš *

Department of Aerospace and Mechanical Engineering, University of Notre Dame, Notre Dame, IN, 46556, USA

ARTICLE INFO

Article history:
Received 18 July 2015
Received in revised form 22 December 2015
Accepted 17 January 2016
Available online 26 February 2016

Keywords:
Computational homogenization
Nonlinear manifold
Reduced order model
Machine learning
Parallel computing

ABSTRACT

A new manifold-based reduced order model for nonlinear problems in multiscale modeling of heterogeneous hyperelastic materials is presented. The model relies on a global geometric framework for nonlinear dimensionality reduction (Isomap), and the macroscopic loading parameters are linked to the reduced space using a Neural Network. The proposed model provides both homogenization and localization of the multiscale solution in the context of computational homogenization. To construct the manifold, we perform a number of large three-dimensional simulations of a statistically representative unit cell using a parallel finite strain finite element solver. The manifold-based reduced order model is verified using common principles from the machine-learning community. Both homogenization and localization of the multiscale solution are demonstrated on a large three-dimensional example and the local microscopic fields as well as the homogenized macroscopic potential are obtained with acceptable engineering accuracy.

1. Introduction

There are abundant applications in engineering where heterogeneous materials composed of different hyperelastic phases experience nonlinear deformations that lead to very large strains. Some practical examples in this category are reinforced rubbers [1,2], soft biological materials [3,4], and solid rocket propellants [5,6], just to name a few. Predicting the mechanical response of such materials from the knowledge of their microstructure and behavior of individual constituents has been a long standing endeavor. In this regard, multiscale methods play an essential role [7,8]. In particular, computational homogenization (CH) is a popular method for bridging scales [9–16]. Two reviews providing more details on CH methods have been published in [10,17].

For nonlinear heterogeneous materials, CH requires solution of two nested nonlinear boundary value problems (BVP). In short, the macroscopic BVP provides boundary conditions for the microscale (localization), and the microscopic BVP yields the average flux (homogenization, i.e. the macroscopic stress tensor at a macroscale material point) and the macroscopic (homogenized) consistent tangent. Although the homogenization and localization processes are concatenated for the fully coupled CH implementation, these processes have distinctly different complexities when used in the context of model reduction, where the full solution over the microstructure is often omitted.

CH is a very powerful technique and provides detailed solutions of both macro- and micro-domains (i.e. both homogenization and localization). However, it is also computationally intensive. Typically, the numerical solution is sought

* Corresponding author.
E-mail address: kmatous@nd.edu (K. Matouš).

http://dx.doi.org/10.1016/j.jcp.2016.01.040
0021-9991/

by employing the finite element method at both scales (i.e. FE^2 implementation) [16,18,19]. To lower this computational expense, the research community has focused on model reduction as it can significantly reduce time and data storage requirements [20–24]. One particularly popular model reduction method is based on proper orthogonal decomposition (POD) [20,21,25]. For example, both homogenization and localization of hyperelastic composites using POD have been performed in 2D by Yvonnet and He [20]. Although very popular, POD is better suited for linear or weakly nonlinear processes (ordinary or partial differential equations) as it relies on a linear combination of few basis vectors [26,27]. Moreover, POD models drift from the FE^2 solution, since the method is directly coupled with the macroscale in terms of the reduced basis. Other popular methods are based on digital database and/or discrete material maps to construct the overall homogenized macro-potentials or to directly homogenize the stress tensor [28–30]. In this category, Temizer and Zhodi [30] and Temizer and Wriggers [29] have introduced a concept of discrete material maps based on virtual material experiments. Here, a range of tri-axial stretches and rotations is applied to create a material homogenization map of the second Piola stress tensor. However, this method can only recover the homogenized response for any new material point. Also, Neural Network (NN) techniques have been employed to obtain approximate constitutive behavior, see Ghaboussi et al. [31], Unger and Konke [32] and Le et al. [33]. Unfortunately, using the NN in high dimensions is impractical [34]. Model calibration is another popular method. In work of Andrade and Tu [35], some key material parameters of a phenomenological plasticity model at the macroscale are calibrated on the fly from microscale computations. Limited mostly to small strain analysis, the Transformation Field Analysis (TFA) and its nonuniform extension (NTFA) have been popular as well [36–38]. Other attempts include proper generalized decomposition [22] and techniques based on the phase-space simplicial interpolation [39]. Recently, a novel Gaussian process emulator of parametrized partial differential equations for single scale analysis has been developed by Xing et al. [40]. In this work, the Isomap and kernel Isomap are used to embed the vectorized spatial and temporal outputs in a low dimensional (feature) space. Unfortunately, most of the works described above are in 2D or limited 3D setting (i.e. small RUC), cannot perform localization of the multiscale response, and/or are limited to small strain analysis.

In this work, we propose a novel multiscale model reduction technique in the context of CH based on nonlinear manifolds learning and computational geometry [41–44]. The proposed technique can perform both homogenization and localization of the material response in 3D finite strains setting with a realistic Representative Unit Cell (RUC). The size of the RUC is established based on statistical analysis of the morphology [45,46]. Next, we use principles from machine-learning [41–44] to construct a digital database of well resolved microscale simulations and their corresponding macroscale loading parameters. The digital database is built from parallel simulations using the in-house *PGFem3D* solver [13,16,47]. Thus, by employing modern high performance computing (HPC) capabilities, the whole database is generated seamlessly. The proposed reduced order model incorporates a complete loading envelope in terms of the principal stretches and the orthogonal principal directions. A uniform discretization of the rotation loading parameters is obtained by incorporating the HEALPix grid [48]. Since the hyperelastic materials are highly nonlinear, we employ a nonlinear manifold learning technique instead of traditional Principal component analysis (PCA) or Multidimensional Scaling (MDS) [49]. Recently, several nonlinear dimension reduction techniques have been proposed. Among these, local techniques (i.e. Locally linear embedding (LLE) [44], Laplacian Eigenmaps [43]) preserve only local geometry and can fail to capture the global pattern, especially when the manifold contains noisy data [49,50]. Moreover, some of the global techniques (i.e. Kernel PCA [51], diffusion maps [52]) are sensitive to the selection of kernels. On the other hand, global technique like Isomap approximately preserves relevant geometrical scales [49]. Therefore, we use Isomap [41] to construct the reduced space, which approximately preserves the microscopic information. Isomap is a global technique for nonlinear manifold reduction that unfolds the solution manifold to a reduced space. Therefore, neighboring data points on the high-dimensional manifold $\mathcal{M}$ (where proximity is described by a geodesic distance) are also neighboring data points in the reduced space $\mathcal{A}$ (where proximity is described by a Euclidean distance). Note that the Isomap technique has been used for a nonlinear dimension reduction of a data-driven stochastic input model [24] and to efficiently construct a Gaussian process emulator of parametrized partial differential equations [34,40]. Due to the highly nonlinear nature of the manifold and curse of dimensionality, we establish the map between the space of macroscopic loading parameters and the reduced space through NN [53–58]. Using the digital database and the manifold-based nonlinear reduced order model (MNROM), we perform both homogenization and localization of the material response for new macroscale loading conditions without any additional large-scale HPC simulations.

This paper is organized as follows. In Section 2, we briefly discuss the theory of computational homogenization for heterogeneous materials. Section 3 is dedicated to the development of the MNROM. In Section 4, we verify the MNROM by using concepts from the machine-learning community and present a numerical example of both homogenization and localization of the multiscale response of a RUC with 95 stiff inclusions. Finally, in Section 5 we draw some conclusions and discuss the issues and scope for further improvement.

2. Multiscale Modeling of Heterogeneous materials

In this section, we briefly summarize the theory of computational homogenization. More details on this theory can be found in [9–11,16,18].

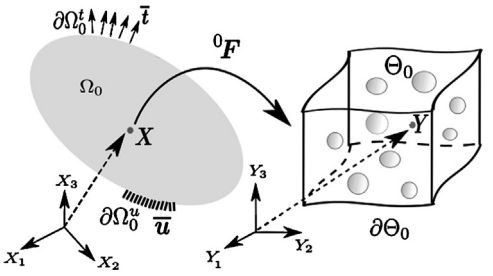

Fig. 1. Schematic of macroscale and microscale domains in theory of computational homogenization.

2.1. Macroscale problem

Consider a body $\Omega_0 \subset \mathbb{R}^3$ consisting of material points $\boldsymbol{X} \in \Omega_0$ as shown in Fig. 1. Let the boundaries $\partial\Omega_0^u$ and $\partial\Omega_0^t$ represent the boundary of applied displacement $\bar{\boldsymbol{u}}$ and tractions $\bar{\boldsymbol{t}}$, respectively. The boundary $\partial\Omega_0$ is decomposed such that $\partial\Omega_0 = \partial\Omega_0^u \cup \partial\Omega_0^t$ with $\partial\Omega_0^u \cap \partial\Omega_0^t = \varnothing$. Next, the deformation ${}^0\boldsymbol{\chi}$ and the deformation gradient ${}^0\boldsymbol{F}$ in the macroscale are defined as

$$\begin{aligned} {}^0\boldsymbol{\chi}(\boldsymbol{X}) &= \boldsymbol{X} + {}^0\boldsymbol{u}(\boldsymbol{X}) && \forall \boldsymbol{X} \in \Omega_0, \\ {}^0\boldsymbol{F}(\boldsymbol{X}) &= \nabla_{\boldsymbol{X}}\, {}^0\boldsymbol{\chi} = \boldsymbol{1} + \nabla_{\boldsymbol{X}}\, {}^0\boldsymbol{u} && \forall \boldsymbol{X} \in \Omega_0, \end{aligned} \tag{1}$$

where $\boldsymbol{1}$ is the second-order identity tensor, and ${}^0\boldsymbol{u}(\boldsymbol{X})$ is the macroscale displacement. Neglecting inertial forces, the macroscale boundary value problem is given by

$$\begin{aligned} \nabla_{\boldsymbol{X}} \cdot {}^0\boldsymbol{P} + {}^0\boldsymbol{b} &= \boldsymbol{0} && \text{in } \Omega_0, \\ {}^0\boldsymbol{P} \cdot {}^0\boldsymbol{N} &= \bar{\boldsymbol{t}} && \text{on } \partial\Omega_0^t, \\ {}^0\boldsymbol{u} &= \bar{\boldsymbol{u}} && \text{on } \partial\Omega_0^u, \end{aligned} \tag{2}$$

where ${}^0\boldsymbol{P} = \partial {}^0W / \partial {}^0\boldsymbol{F}$ is the macroscopic first Piola–Kirchhoff stress tensor, ${}^0W$ is the hyperelastic macroscopic strain energy density function, ${}^0\boldsymbol{b}$ is the macroscale body force, and ${}^0\boldsymbol{N}$ is the unit normal to the surface $\partial\Omega_0^t$. Application of the standard variational procedures leads to the weak form: Find ${}^0\boldsymbol{u} \in \mathcal{V}_{\Omega_0}$ $\left\{ {}^0\boldsymbol{u} : \Omega_0 \to \mathbb{R}^3 |\ \det({}^0\boldsymbol{F}) > 0\ \forall \boldsymbol{X} \text{ in } \Omega_0 \text{ and } {}^0\boldsymbol{u}|_{\partial\Omega_0^u} = \bar{\boldsymbol{u}} \right\}$ such that

$$\mathscr{R}_{{}^0\boldsymbol{u}} := \int_{\Omega_0} {}^0\boldsymbol{P} : (\nabla_{\boldsymbol{X}} \delta\, {}^0\boldsymbol{u})\, \mathrm{d}V - \int_{\partial\Omega_0{}^t} \bar{\boldsymbol{t}} \cdot \delta\, {}^0\boldsymbol{u}\, \mathrm{d}A - \int_{\Omega_0} {}^0\boldsymbol{b} \cdot \delta\, {}^0\boldsymbol{u}\, \mathrm{d}V = 0, \tag{3}$$

holds for variations $\delta\, {}^0\boldsymbol{u}(\boldsymbol{X}) \in \overline{\mathcal{V}}_{\Omega_0}\{\delta\, {}^0\boldsymbol{u} : \Omega_0 \to \mathbb{R}^3,\ \delta\, {}^0\boldsymbol{u}|_{\partial\Omega_0^u} = \boldsymbol{0}\}$. As evident from Equations (2) and (3), we have to know the macroscale strain energy potential ${}^0W$, which is determined by solving the microscale problem, in order to solve the macroscale problem.

2.2. Microscale problem

A microstructure $\Theta_0 \subset \mathbb{R}^3$ consisting of microscale points $\boldsymbol{Y} \in \Theta_0$ as shown in Fig. 1 is locally attached to each macroscale point $\boldsymbol{X} \in \Omega_0$. The microscale deformation $\boldsymbol{\chi}$ and the deformation gradient $\boldsymbol{F}$ are assumed to be functions of both macro and micro variables as

$$\begin{aligned} \boldsymbol{\chi}(\boldsymbol{X}, \boldsymbol{Y}) &= {}^0\boldsymbol{F}(\boldsymbol{X})\boldsymbol{Y} + {}^1\boldsymbol{u}(\boldsymbol{Y}) && \forall \boldsymbol{Y} \in \Theta_0, \\ \boldsymbol{F}(\boldsymbol{X}, \boldsymbol{Y}) &= {}^0\boldsymbol{F}(\boldsymbol{X}) + \nabla_{\boldsymbol{Y}}\, {}^1\boldsymbol{u}(\boldsymbol{Y}) && \forall \boldsymbol{Y} \in \Theta_0, \end{aligned} \tag{4}$$

where ${}^1\boldsymbol{u}(\boldsymbol{Y})$ is the microscale displacement fluctuation. The microscale equilibrium boundary value problem, neglecting body forces and without prescribed tractions, is given by

$$\begin{aligned} \nabla_{\boldsymbol{Y}} \cdot {}^1\boldsymbol{P} &= \boldsymbol{0} && \text{in } \Theta_0, \\ \boldsymbol{\chi} &= {}^0\boldsymbol{\chi} && \text{on } \partial\Theta_0, \end{aligned} \tag{5}$$

where ${}^1\boldsymbol{P} = \partial {}^1W / \partial \boldsymbol{F}$ is the microscopic first Piola–Kirchhoff stress tensor. The microscale free energy density function, ${}^1W$, describes material behavior of interest and is given. The weak form of Equation (5) is derived from the micro-to-macro transition with a particular set of physically applicable and mathematically admissible boundary conditions.

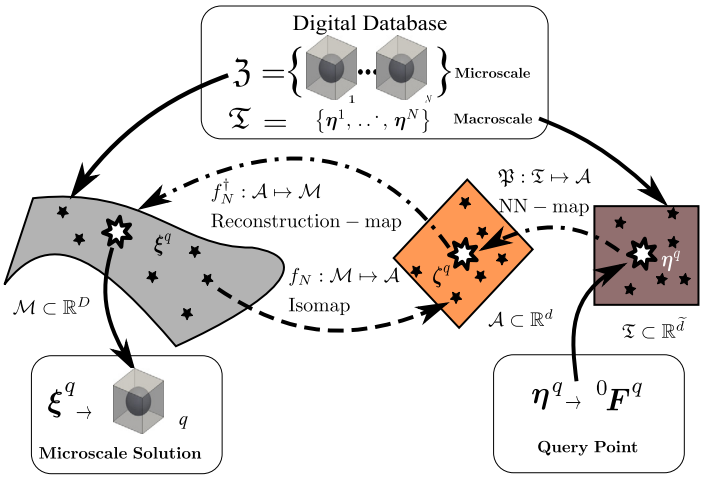

Fig. 2. Concept of the manifold-based nonlinear reduced order model. (For interpretation of the references to color in this figure, the reader is referred to the web version of this article.)

2.3. Micro-to-macro transition

In computational homogenization, the behavior of a material point at the macroscale is linked to the microscale through the Hill–Mandell stationarity condition [9]:

$$\inf_{^0\boldsymbol{u}} {}^0W({}^0\boldsymbol{u}) = \inf_{^0\boldsymbol{u}} \inf_{^1\boldsymbol{u}} \frac{1}{|\Theta_0|} \int_{\Theta_0} {}^1W({}^0\boldsymbol{F} + \nabla_{\boldsymbol{Y}}\, {}^1\boldsymbol{u})\, \mathrm{d}\Theta. \tag{6}$$

Expanding the variation of Equation (6) with respect to $^1\boldsymbol{u}$, we get the weak form of Equation (5). Find $^1\boldsymbol{u} \in \mathcal{V}_{\Theta_0}$ $\{{}^1\boldsymbol{u} : \Theta_0 \to \mathbb{R}^3 | \det(\boldsymbol{F}) > 0 \ \forall \boldsymbol{Y}$ in Θ_0 and $^1\boldsymbol{u}|_{\partial\Theta_0}$ is periodic$\}$ such that

$$\mathscr{R}_{^1\boldsymbol{u}} := \int_{\Theta_0} {}^1\boldsymbol{P} : (\nabla_{\boldsymbol{Y}} \delta\, {}^1\boldsymbol{u}) \mathrm{d}\Theta = 0, \tag{7}$$

is stationary with variation $\delta\,{}^1\boldsymbol{u}(\boldsymbol{Y}) \in \overline{\mathcal{V}}_{\Theta_0}\{\delta\,{}^1\boldsymbol{u} : \Theta_0 \to \mathbb{R}^3,\ \delta\,{}^1\boldsymbol{u}|_{\partial\Theta_0}$is periodic$\}$. As typical in the computational homogenization, we use the periodic boundary conditions for the cell fluctuations, $^1\boldsymbol{u}$ (see Geers et al. [10]).

3. Nonlinear reduced order model

In this section, the macro and microscale coupling is presented in a novel way from nonlinear manifold point of view. Here, a nonlinear manifold is constructed out of the microscale simulations without any assumptions regarding its topology. This novel modeling concept described as a manifold-based nonlinear reduced order model (MNROM) is illustrated in Fig. 2. The MNROM is constructed from a digital database of N detailed microscale simulations (denoted as $\mathfrak{Z}$) and the set of their associated macroscale loading parameters (denoted as $\mathfrak{T}$). An entry in the database is identified by the pair $(\boldsymbol{\eta}^i, \boldsymbol{\xi}^i)$ for $i = 1, \cdots, N$, where $\boldsymbol{\eta}^i$ denotes the ith macroscale loading case and $\boldsymbol{\xi}^i$ denotes data from the ith microscale simulation. When considering hyperelastic response, the database stores the nine components of $\boldsymbol{F}$ (see Equation (4)) for Ne finite elements of the microscale discretization. Thus, each entry $(\boldsymbol{\eta}^i, \boldsymbol{\xi}^i)$ in the database contains $D = 9 \times Ne$ numbers, and the total size of the digital database is $N \times D$.

Using the digital database, we build a high-dimensional manifold $\mathcal{M} \subset \mathbb{R}^D$ (gray region in Fig. 2) containing the set $\mathfrak{Z} = \{\boldsymbol{\xi}^1, \cdots, \boldsymbol{\xi}^N\}$ associated with its corresponding set of macroscale loading conditions $\mathfrak{T} = \{\boldsymbol{\eta}^1, \cdots, \boldsymbol{\eta}^N\} \subset \mathbb{R}^{\widetilde{d}}$, where $\widetilde{d}$ is the number of the physical macroscale loading/controlling parameters. The microscale simulation points, $\boldsymbol{\xi}^i$, are given by the ordered set of the deformation gradients in each element, i.e. $\boldsymbol{\xi}^i = \{\boldsymbol{F}^1, \cdots, \boldsymbol{F}^{Ne}\} \in \mathcal{M}$. Moreover, all other microscale fields (e.g. stress, strain) are derived from $\boldsymbol{F}$. For nearly incompressible materials the MNROM framework will remain similar. Generally, a mixed finite element method is used to handle the nearly incompressible material response [59,60]. In that case pressure/volume variables have to be included in $\boldsymbol{\xi}^i$.

In this work, we use a limited number (N) of parallel simulations using the *PGFem3D* solver [13,16,19,47] to construct the manifold $\mathcal{M}$. The proximity of the points on the manifold are described by the distance metric $\mathcal{D}$ (in terms of L_2 norm), suggesting that the topological space $(\mathcal{M}, \mathcal{D})$ is a metric space, which is bounded, dense, complete and compact [61]. In the limit, $N \to \infty$, the generated manifold $\mathcal{M}$ is smooth and without holes, since the parametric space $\mathfrak{T}$ is without singularity and the manifold is generated through a continuum process.

After constructing the high-dimensional manifold, we look for a low-dimensional Euclidean space $\mathcal{A} \subset \mathbb{R}^d$ (orange region in Fig. 2). This space of lower dimension contains the set of points, $\mathcal{A} = \{\boldsymbol{\zeta}^1, \cdots, \boldsymbol{\zeta}^N\}$, generated from the limited set of simulations $\mathfrak{Z}$, which are associated with the essential macroscale influence parameters ($\boldsymbol{\eta}^i \in \mathfrak{T}$). In this work, we determine the intrinsic dimension, d, of the manifold $\mathcal{M}$, and construct the map $f : \mathcal{M} \mapsto \mathcal{A}$. The Isomap [41] is utilized to construct f_N (see Fig. 2), the discrete version of f, using graph techniques and geodesics, thereby preserving the global structure of $\mathcal{M}$ in $\mathcal{A}$. Thus, near and far points on $\mathcal{M}$ (by geodesic distance) are also near and far on $\mathcal{A}$ (by Euclidean distance).

After establishing all spaces and maps, we would like to perform both homogenization and localization of the microscale response for new macroscale loading conditions, denoted as a macroscale query point $\boldsymbol{\eta}^q \notin \mathfrak{T}$. Moreover, we would like to accomplish this without any additional large-scale HPC simulations. To achieve this goal, we propose to unravel an underlying space of low dimensionality. To close the MNROM, we need to link the low-dimensional parameters to the physical macroscale loading conditions through the map $\mathfrak{P}$. Note that this connection between the low-dimensional space and the physical macroscale parameters is not always straightforward. Here we use the NN [53,56]. Finally, we obtain the microscale solution, $\boldsymbol{\xi}^q$, using the reconstruction map $f_N^\dagger$. In what follows, we summarize briefly the mathematical theories and principles needed to construct a reliable MNROM (see Fig. 2).

3.1. Description of map $f_N : \mathcal{M} \mapsto \mathcal{A}$

As mentioned in the previous section, we establish the map f_N using Isomap [24,41], which generalizes MDS to nonlinear manifolds by replacing the Euclidean distance with approximate geodesic distances on the manifold. In this section, we provide basic mathematical structure of Isomap for completeness of the presentation. The manifold is represented by the graph, G, constructed from the points, $\boldsymbol{\xi}^i$, on the manifold $\mathcal{M}$ using the k-rule, where k nearest neighbors are connected through the graph edges. One of the major components of Isomap is computation of approximate geodesic distances in terms of all-pair shortest paths, and we use Dijikstra algorithm [62]. The approximate geodesic distances computed over the graph G obey the following theorem: Let $\mathcal{M}$ be a compact manifold, embedded in $\mathbb{R}^D$, isometrically equivalent to a convex domain $\mathcal{A} \subset \mathbb{R}^d$ and let some parameters ω_1, ω_2, μ be given in (0, 1). Next, let another parameter $\epsilon > 0$ be chosen such that $\epsilon < s_0$ and $\epsilon \leq (2/\pi) r_0 \sqrt{24\omega_1}$, where s_0 and r_0 are the minimum branch separation and the minimum radius of curvature of the manifold $\mathcal{M}$, respectively. A finite sample set $\{\boldsymbol{\xi}^i\}$ is chosen randomly from the Poisson distribution over the points on $\mathcal{M}$ with the density function α, which has the bounded ratio, $\mathfrak{A} = \alpha_{max}/\alpha_{min}$, where $\alpha_{min} = (k+1)/(V_d(\epsilon/2)^d/2)$ and $\alpha_{min} > 4\log(8V/\mu V_d(\omega_2\epsilon/32\pi)^d))/V_d(\omega_2\epsilon/16\pi)^d$. Here, V is the volume of $\mathcal{M}$ and V_d is the volume of the unit ball in $\mathbb{R}^d$. Now, by providing the conditions, $e^{-(k+1)/4} \leq \mu V_d(\epsilon/4)^d/4V$ and $(e/4)^{(k+1)/2} \leq \mu V_d(\epsilon/8)^d/16\mathfrak{A}V$, and neglecting the boundary effects, we can assert that with the probability at least $1-\mu$ the following inequalities

$$(1-\omega_1) D_M(\boldsymbol{\xi}^i, \boldsymbol{\xi}^j) \leq D_G(\boldsymbol{\xi}^i, \boldsymbol{\xi}^j) \leq (1+\omega_2) D_M(\boldsymbol{\xi}^i, \boldsymbol{\xi}^j), \tag{8}$$

hold on $\mathcal{M}$ for all $\boldsymbol{\xi}^i, \boldsymbol{\xi}^j$, where $D_M(\boldsymbol{\xi}^i, \boldsymbol{\xi}^j) = \inf_\gamma\{\text{length}(\gamma) : \gamma : [0,\ 1] \mapsto \mathcal{M} \text{ and } \gamma(0) = \boldsymbol{\xi}^i, \gamma(1) = \boldsymbol{\xi}^j\}$ is the exact geodesic computed on the Riemannian manifold $\mathcal{M}$. Here, $D_G(\boldsymbol{\xi}^i, \boldsymbol{\xi}^j)$ is the approximate geodesic computed from the graph G [63].

Equation (8) guarantees the asymptotic convergence of the computed approximate geodesics in limiting conditions. Isomap involves the computation of an affinity matrix, $\overline{D}_{ij} = D_G^2(\boldsymbol{\xi}_i, \boldsymbol{\xi}_j)$, from the data set $\mathfrak{Z}$. Once this is done, the matrix $\overline{D}$ is transformed to the double-centered matrix $\widetilde{D}$, which reads

$$\widetilde{D}_{ij} = -\frac{1}{2}\left(\overline{D}_{ij} - \frac{1}{N}\mathfrak{D}_i - \frac{1}{N}\mathfrak{D}_j + \frac{1}{N^2}\sum_k \mathfrak{D}_k\right), \tag{9}$$

where $\mathfrak{D}_i$ is the ith row sum of the affinity matrix $\overline{D}$ ($\mathfrak{D}_i = \sum_j \overline{D}_{ij}$). Then, the embedding is constructed by $\zeta_k^i = \sqrt{\sigma_k}\, v_i^k$, where σ_k is the kth eigenvalue and $\boldsymbol{v}^k$ is the corresponding eigenvector of $\widetilde{D}$. Here, ζ_k^i is the kth component of $\boldsymbol{\zeta}^i$ out of d components, and v_i^k is the ith component of $\boldsymbol{v}^k$ out of N components.

Truncation in the decaying spectrum is done by applying the Beardwood–Halton–Hammersley (BHH) theorem [64]. Let $\mathcal{M}$ be a smooth compact d-dimensional manifold embedded in $[0,\ 1]^D \subset \mathbb{R}^D$ through the diffeomorphism $f^{-1} : \mathbb{R}^d \mapsto \mathcal{M}$ and assume $2 \leq d \leq D$ and $0 < \Upsilon < d$. Now suppose that $\mathfrak{Z}$ is the set of independent and identically distributed random vectors which lie on $\mathcal{M}$ having uniform density Γ with respect to a Lebesgue measure $\mu_{\mathcal{M}}$ on $\mathcal{M}$. Next, assume that the edge length $D_G(\boldsymbol{\xi}^i, \boldsymbol{\xi}^j)$ of the undirected graph, G, converging to $\|f(\boldsymbol{\xi}^i) - f(\boldsymbol{\xi}^j)\|_{L_2}$ as $N \to \infty$. Then, the length functional $L_\Upsilon^{\mathcal{M}}(\mathfrak{Z})$ of the geodesic minimal spanning tree (*GMST*) of graph G satisfies

$$\lim_{N\longrightarrow\infty} L_\Upsilon^{\mathcal{M}}(\mathfrak{Z})/N^{(d'-\Upsilon)/d'} = \begin{cases} \infty & \text{if } d' < d \\ \beta_d C & \text{if } d' = d \\ 0 & \text{if } d' > d, \end{cases} \tag{10}$$

where β_d is a constant that is independent of the probability distribution of $\mathfrak{Z}$, and C is defined on $\mathcal{M}$ as

$$C = \int_{\mathcal{M}} \Gamma^{((d-\Upsilon)/d)}(\boldsymbol{\xi}) g^{-\Upsilon/d}(f^{-1}(\boldsymbol{\xi})) \mu_{\mathcal{M}}(\mathrm{d}\boldsymbol{\xi}). \tag{11}$$

Here, $g = \sqrt{\det[\boldsymbol{J}_{\mathrm{f}}^{\mathrm{T}}\boldsymbol{J}_{\mathrm{f}}]}$ with $\boldsymbol{J}_f$ being the Jacobian of f, and $\boldsymbol{\xi}$ is a generic vector on $\mathcal{M}$. Moreover, the mean $(E[L_\Upsilon^{\mathcal{M}}(\mathfrak{Z})]/N^{(d'-\Upsilon)/d'})$ converges to the same limit.

Now the length functional $L_\Upsilon^{\mathcal{M}}$ provides a means of estimating the intrinsic dimension of the manifold. Defining $l_N = \log(L_\Upsilon^{\mathcal{M}})$ gives the following approximation

$$l_N = a\log(N) + b + \epsilon_N, \tag{12}$$

where $a = \frac{d-\Upsilon}{d}$, $b = \log(\beta_d C)$, and ϵ_N is the residual error that approaches zero with increasing N. The intrinsic dimensionality d can be estimated by finding the length functional for different number of samples and subsequently finding the best fit for (a, b). Once d is computed, embedding can be constructed by taking first d eigenvalues and eigenvectors [64]. It can be shown that convergence takes place asymptotically for an isometric map. To finalize the description of Isomap, we provide simple implementation procedure in Algorithm 1.

Algorithm 1 Isomap.

1: Construct neighborhood graph, G: *Compute L_2 distance between all pairs ($\boldsymbol{\xi}^i$, $\boldsymbol{\xi}^j$). Apply k-rule to select the k-neighbors of all $\boldsymbol{\xi}^i$. Every $\boldsymbol{\xi}^i$ will have k-edges with Euclidean distance as the edge weight.*
2: Compute all-pair shortest paths in G: *Use Floyd/Dijikstra algorithm [62,65] to compute all-pair shortest paths and store the squared value of each shortest path in $\overline{D}$ matrix. Compute double centered matrix $\widetilde{D}$ from $\overline{D}$ given by Equation (9).*
3: Determine the intrinsic dimension: *Use BHH theorem and follow Equations (10)–(12) to determine the intrinsic dimension of manifold d.*
4: Construct the reduced-dimensional space: *Apply classical MDS technique on $\widetilde{D}$. Compute d largest eigenvalues, σ_k, and corresponding eigenvectors, $\boldsymbol{v}^k$ of $\widetilde{D}$. The reduced dimensional space is obtained as $\zeta_k^i = \sqrt{\sigma_k}\, v_i^k$.*

3.2. Description of inverse Map $f_N^\dagger : \mathcal{A} \mapsto \mathcal{M}$

Although, the Isometric map can be constructed explicitly [42], in our work, the map f_N is without an explicit form and does not have any explicit inverse. In order to predict the micro-structural response from the reduced dimensional parameters, we numerically construct an approximation to the inverse map through regression [66]. First, we describe the basic mathematical property of inverse map and then we discuss several inverse map candidates that were used in Section 4 (Numerical Examples). Consider a simulation point $\boldsymbol{\xi}^i \in \mathcal{M}$ and its corresponding point in the reduced space $\boldsymbol{\zeta}^i \in \mathcal{A}$, where $\boldsymbol{\zeta}^i = f(\boldsymbol{\xi}^i)$. Next, we assume that the discrete map f_N converges to the limiting map, i.e. $f_N(\boldsymbol{\xi}^i) = f(\boldsymbol{\xi}^i)$ for $i = 1, \ldots, N$. Thus, the approximate inverse, $f_N^\dagger$, is constructed from a finite set of points such that $\forall \boldsymbol{\zeta} \in f(\mathcal{M})$ the inverse map $f_N^\dagger$ converges to the exact inverse f^{-1} at the limit ($\lim_{N\to\infty} f_N^\dagger(\boldsymbol{\zeta}) = f^{-1}(\boldsymbol{\zeta})$). The approximate inverse map for a point of interest $\boldsymbol{\zeta}^q$ (query point) is denoted as $\boldsymbol{\xi}^q = f_N^\dagger(\boldsymbol{\zeta}^q)$ (see Fig. 2) and is constructed in the sense of non-parametric regression [67].

One of the basic approaches for creating this reconstruction map over the manifold $\mathcal{M}$ is to use the conditional probability density $P^i(\boldsymbol{\xi}^i|\boldsymbol{\zeta}^q)$:

$$\boldsymbol{\xi}^q = \sum_{i=1}^{N} \boldsymbol{\xi}^i P^i(\boldsymbol{\xi}^i|\boldsymbol{\zeta}^q). \tag{13}$$

Many models emanate from Equation (13) since it provides generic description [67]. One simple approach of finding inverse is by finding the set of k-nearest neighbors (points) $\mathfrak{H}_\zeta^q = \{\boldsymbol{\zeta}^{q,1}, \ldots, \boldsymbol{\zeta}^{q,k}\}$ of $\boldsymbol{\zeta}^q$ and the corresponding set of simulation points $\mathfrak{H}_\xi^q = f_N^{-1}(\mathfrak{H}_\zeta^q) = \{\boldsymbol{\xi}^{q,1}, \ldots, \boldsymbol{\xi}^{q,k}\}$ on the manifold $\mathcal{M}$. Using the fact that $\mathcal{A}$ is isometrically embedded in $\mathcal{M}$, the point $\boldsymbol{\xi}^q \in \mathcal{M}$ is obtained by (see Ref. [24])

$$\boldsymbol{\xi}^q = \frac{\sum_{i=1}^{k} \boldsymbol{\xi}^{q,i}(1/l^{q,i})}{\sum_{i=1}^{k}(1/l^{q,i})}, \tag{14}$$

where $l^{q,i} = \|\boldsymbol{\zeta}^q - \boldsymbol{\zeta}^{q,i}\|_{\mathrm{L}_2}$. Note that Equation (14) is equivalent to Equation (13) with $P^i(\boldsymbol{\xi}^i|\boldsymbol{\zeta}^q) = 1/l^{q,i}/\sum_{i=1}^{k}(1/l^{q,i})$ and sum is truncated within k-nearest points. This method is commonly known as local linear interpolation. Another simple, but often used interpolation method, is nearest neighbor averaging. For this method, $P^i(\boldsymbol{\xi}^i|\boldsymbol{\zeta}^q) = 1/k$ with summation truncation up to k-nearest points. In the Nadaraya–Watson approach [68], regression is the probability estimation of the data as follows

$$\boldsymbol{\xi}^q = \sum_{i=1}^{N} \boldsymbol{\xi}^i \mathfrak{K}\left(\frac{\boldsymbol{\zeta}^i - \boldsymbol{\zeta}^q}{h(N)}\right) \Big/ \sum_{i=1}^{N} \mathfrak{K}\left(\frac{\boldsymbol{\zeta}^i - \boldsymbol{\zeta}^q}{h(N)}\right), \tag{15}$$

where $\mathfrak{K}(.,.)$ is the kernel density and $h(N)$ is the scale associated with the distribution of data. The factor $\mathfrak{K}\left(\frac{\boldsymbol{\zeta}^i-\boldsymbol{\zeta}^q}{h(N)}\right) / \sum_{i=1}^{N} \mathfrak{K}\left(\frac{\boldsymbol{\zeta}^i-\boldsymbol{\zeta}^q}{h(N)}\right)$ can be interpreted as the conditional probability density $P^i(\boldsymbol{\xi}^i|\boldsymbol{\zeta}^q)$. Unfortunately, the Nadaraya–Watson

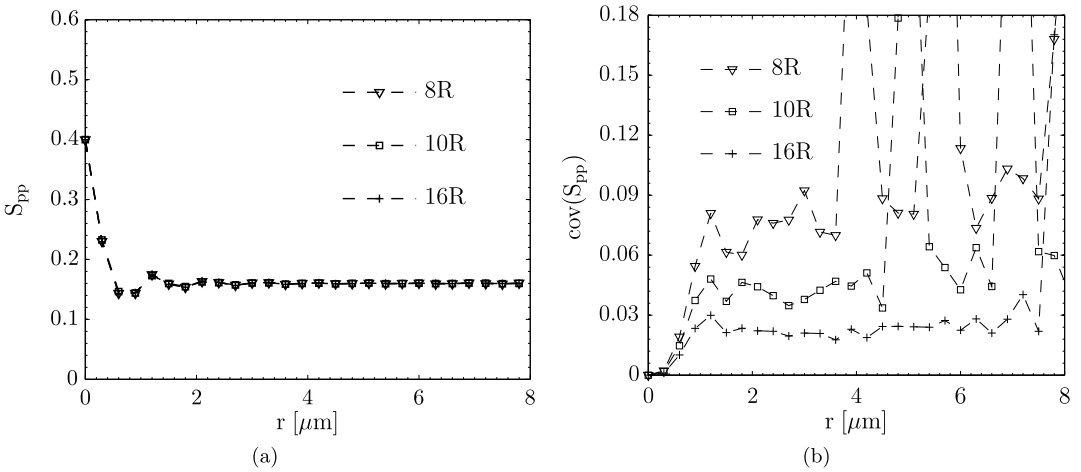

Fig. 3. Statistical analysis of the RUC. (a) Isotropic second-order particle-to-particle probability function. (b) Directional covariance of the second-order particle-to-particle probability.

type regression is highly sensitive to kernel selection. Also most of the generic kernels are highly scale (h_N) dependent. Moreover, this technique suffers when neighborhood of the query point is very sparse.

The reproducing kernel map construction (see [69]) is in general very robust and can be done using the Radial Basis Function (RBF)

$$\xi_j^q = \sum_{i=1}^{N} \theta_j^i \Re(\boldsymbol{\zeta}^i, \boldsymbol{\zeta}^q). \tag{16}$$

Here, ξ_j^q is the jth component of the solution vector ($\boldsymbol{\xi}^q$) and the reproducing kernel, $\Re(\boldsymbol{\zeta}^i, \boldsymbol{\zeta}^q) = \varrho(\|\boldsymbol{\zeta}^i - \boldsymbol{\zeta}^q\|)$, is a RBF. The coefficients θ_j^i are determined using the training data set $(\boldsymbol{\zeta}^i, \boldsymbol{\xi}^i)$ as follows

$$\begin{bmatrix} \theta_1^1 & \cdots & \theta_D^1 \\ \vdots & \ddots & \vdots \\ \theta_1^N & \cdots & \theta_D^N \end{bmatrix} = \begin{bmatrix} \Re(\boldsymbol{\zeta}^1, \boldsymbol{\zeta}^1) & \cdots & \Re(\boldsymbol{\zeta}^1, \boldsymbol{\zeta}^N) \\ \vdots & \ddots & \vdots \\ \Re(\boldsymbol{\zeta}^N, \boldsymbol{\zeta}^1) & \cdots & \Re(\boldsymbol{\zeta}^N, \boldsymbol{\zeta}^N) \end{bmatrix}^{-1} \begin{bmatrix} \xi_1^1 & \cdots & \xi_D^1 \\ \vdots & \ddots & \vdots \\ \xi_1^N & \cdots & \xi_D^N \end{bmatrix}. \tag{17}$$

The robustness and the stability of this method depend on the selection of the kernel function [70]. In this work, we have used the bi-harmonic function ($\varrho(\|\boldsymbol{\zeta}^i - \boldsymbol{\zeta}^q\|) = \|\boldsymbol{\zeta}^i - \boldsymbol{\zeta}^q\|$) for the inverse map.

Finally, we note that nonuniqueness of the inverse map can be mitigated by the Bayesian framework [71]. However, this will lead to an expensive process especially for very high dimensional data.

3.3. Description of map $\mathfrak{P} : \mathfrak{T} \mapsto \mathcal{A}$

Finally, the last map that needs to be described in this technique (see Fig. 2) is the relationship between the macroscale loading parameter space $\mathfrak{T}$ and the low-dimensional isometric space $\mathcal{A}$. Note that the connection between the reduced space, $\mathcal{A}$, and the space of physical macroscale parameters, $\mathfrak{T}$, is not straightforward for nonlinear problems. In this work, the map between the reduced space, $\mathcal{A}$, and the macroscale loading parameter space, $\mathfrak{T}$, is established through the use of NN [53] by minimizing the mean-square error between the reduced space, $\mathcal{A}$, and the approximate output of the NN denoted here as $\overline{\mathcal{A}}$.

4. Numerical example

In this work, we are interested in the behavior of randomly configured (statistically isotropic) particulate materials. Computational homogenization introduced in Section 2 relies on the concept of scale separation and existence of a representative microscopic cell. In order to select the size of the representative microscopic cell, we use a statistical approach [45,46]. In this approach, we generate three different cell sizes, $8R$, $10R$ and $16R$, where R is the radius of the inclusion. Here, the inclusions are monodisperse hard spheres with radius $R = 0.5$ μm. The cells are generated using the packing algorithm *Rocpack* [72].

Fig. 3 shows the isotropic second order probability function, S_{pp} (i.e. particle–particle probability function), and its directional covariance. As typical, larger cells preserve more structure and are more representative. From this statistical study,

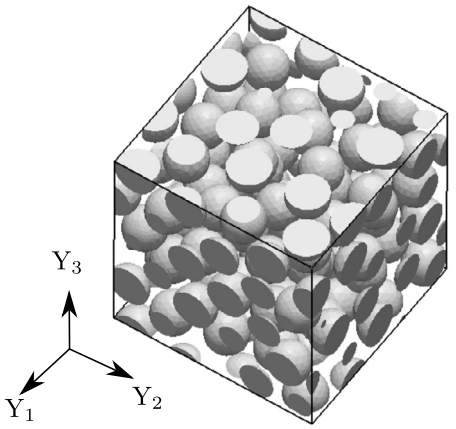

Fig. 4. RUC with side length of $l_{RUC} = 10R = 5$ μm. The cell contains 95 hard spherical particles with 1 μm diameter.

Table 1
Mooney–Rivlin material properties.

Material	E [MPa]	ν	κ [MPa]	G [MPa]	μ_{01} [MPa]	μ_{10} [MPa]
Particle	5e3	0.25	3.33e3	2e3	5e2	5e2
Matrix	50	0.35	55.56	18.52	4.63	4.63

we have constructed a RUC with a side length of $l_{RUC} = 10R = 5$ μm containing 95 particles, with the covariance error below 5%. More details on construction of a RUC can be found in [45,46]. Fig. 4 shows the geometry of the cell used in this work. After a convergence study, the RUC is discretized with 96,252 nodes and 486,051 elements, which results in 250,035 nonlinear degrees of freedom to solve the micro-problem (see Equation (7)).

With the RUC established, appropriate constitutive models at the microscale are selected. We use an isotropic hyperelastic strain-energy density function similar to the Mooney–Rivlin hyperelastic model and employ the volumetric and deviatoric split, ${}^1W(\boldsymbol{C}) = {}^1W_{\mathrm{C}}(\widehat{\boldsymbol{C}}) + {}^1W_{\mathrm{J}}(J)$, with

$$
\begin{aligned}
{}^1W_{\mathrm{C}}(\widehat{\boldsymbol{C}}) &= \mu_{10}\left[\mathrm{tr}(\widehat{\boldsymbol{C}}) - 3\right] + \frac{\mu_{01}}{2}\left[(\mathrm{tr}\widehat{\boldsymbol{C}})^2 - \widehat{\boldsymbol{C}} : \widehat{\boldsymbol{C}} - 6\right], \\
{}^1W_{\mathrm{J}}(J) &= \frac{\kappa}{2}\left[\exp(J-1) - \ln(J) - 1\right].
\end{aligned} \tag{18}
$$

In Equation (18), $J = \det(\boldsymbol{F})$ is the Jacobian of the deformation, $\widehat{\boldsymbol{C}} = J^{-2/3}\boldsymbol{C}$ is the deviatoric right Cauchy–Green deformation tensor, μ_{10} and μ_{01} are the shear moduli, and κ is the bulk modulus. The associated material properties of the microscale constituents are provided in Table 1.

4.1. Macroscale loading parameters $\mathfrak{T}$ and construction of reduced space $\mathcal{A}$

The microstructure is loaded, as in strain driven CH, by the macroscopic deformation gradient, ${}^0\boldsymbol{F}(\boldsymbol{X})$. Using the polar decomposition, ${}^0\boldsymbol{F} = {}^0\boldsymbol{R}\,{}^0\boldsymbol{U}$, we obtain

$$
{}^0\boldsymbol{U} = {}^0\lambda_1({}^0\boldsymbol{e}^1 \otimes {}^0\boldsymbol{e}^1) + {}^0\lambda_2({}^0\boldsymbol{e}^2 \otimes {}^0\boldsymbol{e}^2) + {}^0\lambda_3({}^0\boldsymbol{e}^3 \otimes {}^0\boldsymbol{e}^3), \tag{19}
$$

where ${}^0\lambda_i \in (0, \infty]$ are components of the principal stretch and ${}^0\boldsymbol{e}^i$ are the orthogonal principal directions generated by the axis-angle representation. Recognizing that the microscopic response is invariant to the macroscopic rotation, ${}^0\boldsymbol{R}$, we proceed forward with ${}^0\boldsymbol{U}$ being the key loading parameter.

In order to parameterize the principal directions associated with the principal stretches, we exploit the symmetry of the tensor product. The axis ${}^0\boldsymbol{e}^1$ is constructed from the position vectors of points on the unit hemisphere ($X^3 \geq 0$ in Fig. 5), which are characterized by the angles $\varphi^1 \in [0, 2\pi]$, $\varphi^2 \in [0, \frac{\pi}{2}]$. We use the HEALPix grid [48] to obtain a uniform distribution of points on the hemisphere. For the rotation about the axis ${}^0\boldsymbol{e}^1$ (see Fig. 5), we parametrize the angle, φ^3 in $[0, \frac{\pi}{2})$. Thus, we use the set $\mathfrak{T} = \{{}^0\lambda_1, {}^0\lambda_2, {}^0\lambda_3, \varphi^1, \varphi^2, \varphi^3\}$ to represent the space of ${}^0\boldsymbol{U}$, and each loading condition $\boldsymbol{\eta}^i \in \mathfrak{T}$ is described by six generators (see Section 3). In this work, the digital database is divided into four separate loading segments (referred to as Modes 1–4) and is constructed as described in Table 2.

Bifurcation is a common phenomenon in nonlinear continuum mechanics and appears even in seemingly simple problems involving fairly standard constitutive models [60,73]. We remark that capturing limit and bifurcation points requires a special numerical treatment [74]. Thus, multiple MNROMs would have to be constructed and analyzed to study the bifurcated solutions. We do not perform such analysis in this work. However, when working with random materials with many

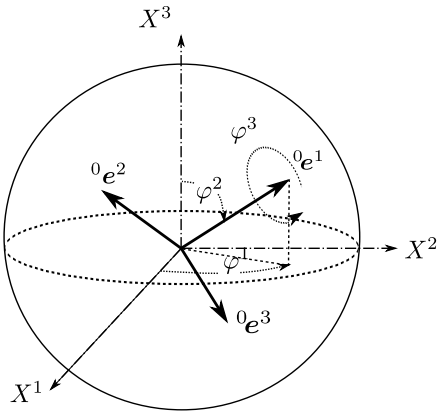

Fig. 5. Schematic of the rotation parameters.

Table 2
Description of the macroscale loading modes.

Loading case	Description	No. simulations
Mode 1	${}^0\lambda^1 \geq 0,\ {}^0\lambda^2 \geq 0,\ {}^0\lambda^3 \geq 0$	4032
Mode 2	${}^0\lambda^1 \leq 0,\ {}^0\lambda^2 \geq 0,\ {}^0\lambda^3 \geq 0$	4032
Mode 3	${}^0\lambda^1 \leq 0,\ {}^0\lambda^2 \leq 0,\ {}^0\lambda^3 \geq 0$	4032
Mode 4	${}^0\lambda^1 \leq 0,\ {}^0\lambda^2 \leq 0,\ {}^0\lambda^3 \leq 0$	4032

inclusions, the microstructure introduces geometrical (morphological) imperfections that guide the solution path. Moreover, we use displacement driven CH where the macro-deformation is uniquely prescribed.

After a discretization study, we have approximated principal stretches with a $4 \times 3 \times 3$ uniform grid over 10% stretch interval. This leads to large strain conditions. Moreover, we have used 112 distinct rotations to generate the bases, $[{}^0\boldsymbol{e}^1\ {}^0\boldsymbol{e}^2\ {}^0\boldsymbol{e}^3]$. In this work, we simply use a uniform discretization of the input parameters. We start with an initial guess of zero displacement for each mode, and then simulations proceed by traversing from one loading condition to another. Note that this discretization leads to 4032 solutions of the microscale boundary value problem, Equation (7), for each mode ($N = 4 \times 4032$). Although this is a moderately large number of simulations, all simulations are executed in parallel using the parallel *PGFem3D* solver [13,16,47]. Thus, the whole database can be generated quickly given current HPC capabilities. In our work, we have not encountered numerical difficulties in solving the nonlinear BVP (Eq. (7)). When such numerical difficulties occur, the manifold would experience coverage deficiency that would have to be mitigated by conducting extra numerical simulations in regions of convergence impediment. Note that even this seemingly large number of simulations still leads to a very sparse manifold $\mathcal{M}$ considering the ambient high-dimensionality ($D = 9 \times Ne$), which is commonly referred to as the curse of dimensionality.

As anticipated, multiple loading conditions can have the similar BVP solution, which leads to non-uniqueness of the deformation gradient in the manifold construction. For example, pure volumetric deformations are rotation invariant. Although, from Isomap point of view redundant data points are ineffectual, we retain all nonunique solutions for the enrichment of the model.

After constructing the digital database, Isomap gives a reduced dimensionality of $d = 6$ for each loading mode, down from the complete solution manifold with the dimension of $D = 4{,}374{,}459$. The residual correlation coefficient between the Euclidean and the approximate geodesic distances of the complete solution manifold are below 0.1 for all modes (see Fig. 6). Moreover, near perfect exponential convergence is obtained. Note that Modes 2 and 3 are more nonlinear and have initially higher residual variance. The effect of this nonlinearity will be discussed in Section 4.5.

4.2. Verification of inverse map $f_N^\dagger$

In order to understand the errors associated with methods used for constructing the approximate inverse map between the complete and reduced spaces, $f_N^\dagger$, we exploit the isometric nature of Isomap, which guarantees preservation of the neighborhood structure. To quantify the error, we use the common 'leave-one-out' procedure from the machine learning community [69]. This procedure consists of removing a single point from the manifold construction, interpolating this removed point from the reduced manifold, and comparing the interpolated point to the known one. We have applied this procedure to 10% of the total 4,032 points (selected randomly) for each loading mode.

The error associated with removing one of these random points from the manifold is quantified by considering the local (localization) error ($\mathcal{E}_r$) computed at micro-points $\boldsymbol{Y}$ (i.e. each finite element in the RUC discretization). This error measure is defined as

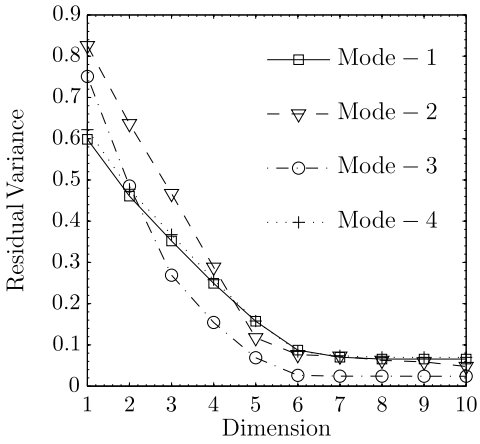

Fig. 6. Isomap dimensionality.

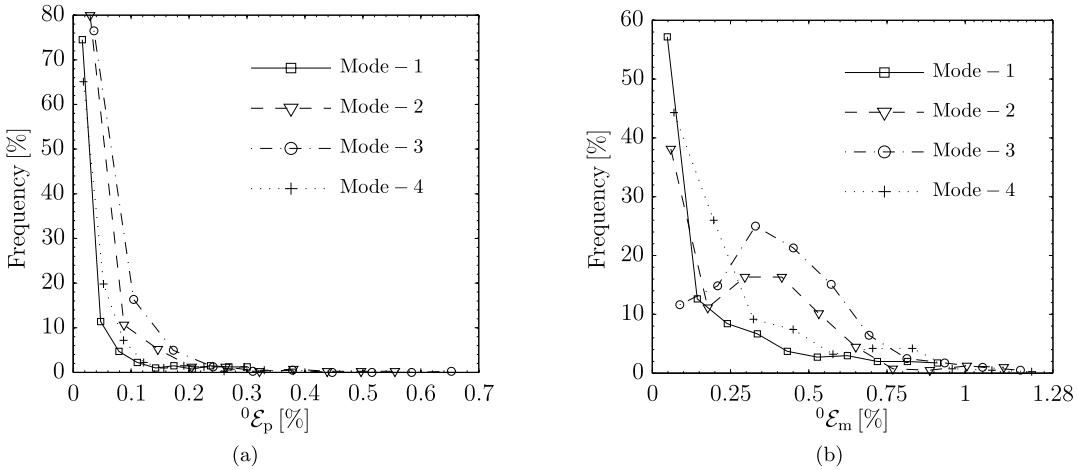

Fig. 7. Distribution of the volume averaged error (homogenization) given by Equation (21) for randomly selected 10% of points from database (one-out cases). (a) Particle. (b) Matrix.

$$\mathcal{E}_r = \frac{\|\boldsymbol{F}_r^{ROM} - \boldsymbol{F}_r^{FEM}\|_{\mathcal{F}}}{\|\boldsymbol{F}_r^{FEM}\|_{\mathcal{F}}} \times 100\,[\%], \tag{20}$$

where $\boldsymbol{F}_r^{ROM}$ and $\boldsymbol{F}_r^{FEM}$ are the deformation gradients computed from the regression model as described in Section 3.2 and the Finite Element Method (FEM) simulation, respectively. Here, we use the Frobenius norm ($\|\bullet\|_{\mathcal{F}}$). The subscript r represents a material phase (particle or matrix). In order to quantify the cumulative error for a single simulation point removed from the manifold, the following volume averaged (homogenization) error, $^0\mathcal{E}_r$, reads

$$^0\mathcal{E}_r = \frac{\frac{1}{\Theta_0}\int_{\Theta_r} \mathcal{E}_r \mathrm{d}\Theta}{\|^0\boldsymbol{F}_r\|_{\mathcal{F}}}, \tag{21}$$

where $^0\boldsymbol{F}_r = \frac{1}{\Theta_0}\int_{\Theta_r} \boldsymbol{F}\, \mathrm{d}\Theta$.

Upon experimenting with several regression schemes (Equations (13)–(15)), we have used the RBF model given in Equation (16). Note that simple local linear interpolation, Eq. (15), was not accurate for many points on the manifold because of the neighborhood sparsity. While implementing the reproducing kernel map given by Equation (16), we solve Eq. (17) to determine θ_j^i coefficients for all dimensions (D) involving all 4032 training data-points for each mode.

Figs. 7(a) and 7(b) show the cumulative error (homogenization) of the leave-one-out cases for the particles and matrix, respectively. Error characteristics of the inverse map are shown in Table 3. Note that the largest error over all one-out points occurs for Mode 3 (circular markers in Fig. 7(a) and 7(b)). Therefore, further localization error analysis is conducted only for Mode 3.

We plot the distributions of the element-wise (localization) error, Equation (20), in Figs. 8(a) and 8(b) for the matrix and particles, respectively. To simplify the interpretation of the results, we plot the mean and standard deviation of the localiza-

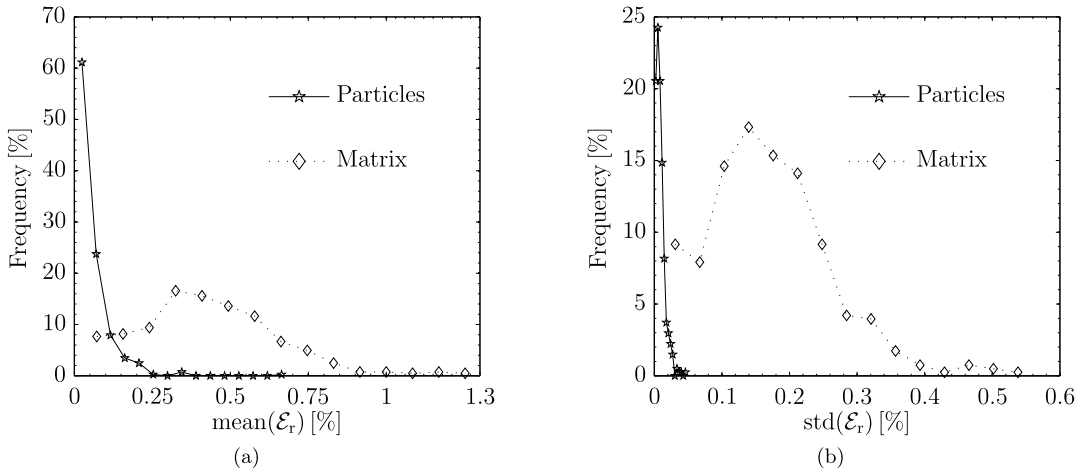

Fig. 8. Distribution of the local error (localization) given by Equation (20) for randomly selected 10% of points from Mode 3 (one-out cases). (a) Mean error of the deformation gradient field. (b) Standard deviation of the deformation gradient field.

Table 3
Quality of the regression model for construction of the inverse map, $f_N^{\dagger}$, for all modes computed from Equation (21).

Loading cases		Min. [%]	Max. [%]	Mean [%]	Median [%]
Mode 1	Particle	1.8410e−07	0.3161	0.0314	0.0028
	Matrix	4.6437e−07	0.9589	0.1586	0.0314
Mode 2	Particle	2.6032e−06	0.5846	0.0424	0.0226
	Matrix	4.8607e−06	1.1823	0.2560	0.2395
Mode 3	Particle	1.6000e−03	0.6870	0.0530	0.0381
	Matrix	2.7100e−02	1.2367	0.4002	0.3827
Mode 4	Particle	3.0786e−04	0.3472	0.0386	0.0181
	Matrix	5.7000e−03	1.2755	0.2309	0.1553

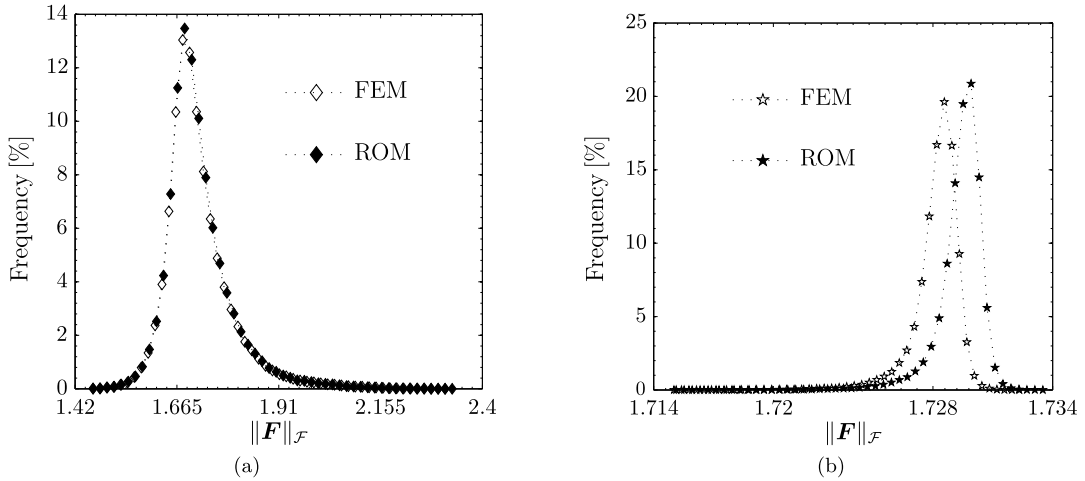

Fig. 9. Distribution of $\|\boldsymbol{F}\|_{\mathcal{F}}$ from FEM and MNROM. (a) Over matrix. (b) Over particle.

tion error, $\mathcal{E}_r$, computed over the finite element field (i.e. deformation gradient) given in Equation (20) from leave-one-out points. As can be seen, the maximum localization error occurs in the compliant matrix and is more uniformly distributed. Moreover, all errors (both localization and homogenization) are below 1.5%, which demonstrates good construction of our inverse map.

Finally, to understand the local distribution of the deformation gradient magnitude, we plot $\|\boldsymbol{F}\|_{\mathcal{F}}$ in Figs. 9(a) and 9(b). This distribution is generated for data point, $\boldsymbol{\xi}^i$, with mean($\mathcal{E}_r$) = 1.2367% error from Mode 3. Note that these distributions

Table 4
Neural Network regression performance.

Loading case	Regression coefficient	Performance	Target range
Mode 1	0.99879	5.3934	[−150 150]
Mode 2	0.99894	9.3900	[−220 220]
Mode 3	0.99940	5.3042	[−220 220]
Mode 4	0.99914	3.8544	[−150 150]

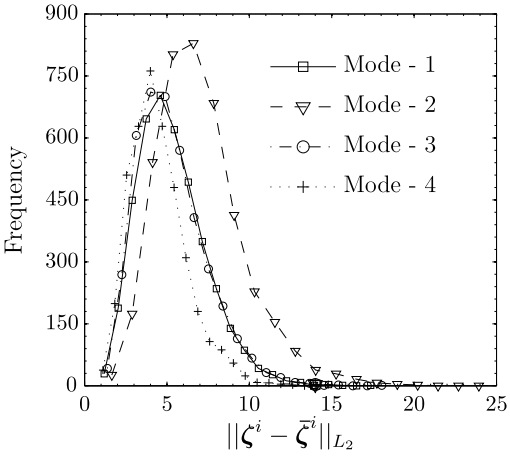

Fig. 10. Distribution of Neural Network output error compared to reduced space over entire dataset.

obtained through the regression model (see Section 3.2) match the simulation data extremely well. This indicates that accurate microscale fields are obtained from the reduced manifold using our approximate inverse map, $f_N^{\dagger}$.

4.3. Verification of map $\mathfrak{P}$

To complete the MNROM framework, a map also needs to be established between the reduced space $\mathcal{A}$ and the space of macroscopic loading parameters $\mathfrak{T}$. This map is denoted as $\mathfrak{P}$ (see Fig. 2). Since the process of generating data is highly nonlinear, and the neighborhood structure is destroyed due to the curse of dimensionality (recall that $D = 9 \times Ne = \mathcal{O}(10^6)$), we have constructed the map using NN. As discussed in Section 4.1, we are retaining all solutions which leads to higher predictive capability of the NN model. Multilayer feed-forward networks are very efficient at establishing a large class of measurable maps [55]. Since NN is not an explicit map, the performance of the model depends on many parameters. The number of hidden layers and the number of nodes are important issues for better generalization of the model. The architecture of NN used in this work is two hidden layers with 70 nodes per layer for Modes 1, 2 and 4. Mode 3 contains 75 nodes per layer. This selection is guided by the fact that in general a two-layer NN is sufficient to capture nonlinear features [56].

In this work, the NN Toolbox in MATLAB is utilized [53]. The target-function/error is computed by a mean-square error (MSE). We have used common regularization techniques to optimize the regression model [53]. Furthermore, we have used the Bayesian model for multilayer feed-forward networks [53,57] to train the data. The quality of the regression is summarized in Table 4 for all loading modes. Note that the linear regression coefficient is close to one for all cases indicating a good fit. The performance of a NN should be judged relative to the range of the target space, and the MSE performance is on the order $\mathcal{O}(10^{-4})$ in the range $[-1, 1]$.

To investigate further the quality of this map, the error between $\mathcal{A}$ and $\overline{\mathcal{A}}$, which is the output of NN, is illustrated for each of the loading modes in Fig. 10. The geometric interpretation of this error is simply the Euclidean distance between points in $\mathcal{A}$ and the corresponding points in $\overline{\mathcal{A}}$. Fig. 10 also shows that the average shift of the MNROM solution from the corresponding FEM along the manifold $\mathcal{M}$ is around 5 units (around 7 units in Mode 2), and 4.57% of points are more than 10 units in terms of geodesic distance. Moreover, the spread of the data is large as indicated in Table 4 (note the range of the six-dimensional space $\mathcal{A}$ (Target Range)), and this difference is accumulated over $D = 4{,}374{,}459$ components. Therefore, the map established by means of NN provides a useful transformation of the macroscale physical parameters to the reduced space, and it will not deteriorate the physics unless the process is highly sensitive to the macroscale loading parameters. We will comment on the accuracy and applicability of NN further in the next section.

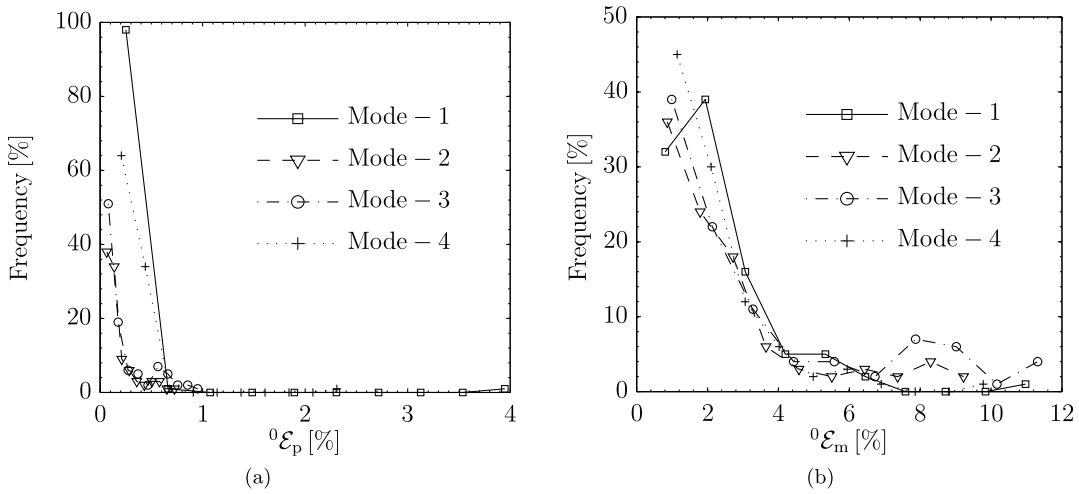

Fig. 11. Distribution of the volume averaged error (homogenization) given by Equation (21) of the 100 randomly selected query points in each mode. (a) Particle. (b) Matrix.

4.4. Verification of complete MNROM framework

After creating the digital database and establishing maps between the high-dimensional space of microscale data, the reduced space, and the macroscale loading parameters, the MNROM framework (see Fig. 2) can be used to compute macroscale (homogenization) as well as microscale (localization) fields for a given macroscale input that is not present in the digital database. The input query is denoted as $\boldsymbol{\eta}^q$, which corresponds to a point in $\mathfrak{T}$ (the macroscale loading parameters). This query point is mapped to the reduced space $\mathcal{A}$ using the map $\mathfrak{P}$ derived from the NN. Finally, the microscale data is obtained using the approximate inverse, $f_N^{\dagger}$. We exercise this entire framework by computing the microscale response, $\boldsymbol{\xi}^q$, of 100 random query points, $\boldsymbol{\eta}^q$, for each mode taken within the range of the $\mathfrak{T}$ space. A total of 400 random query points are generated (i.e. 100 in each mode) from a uniform distribution over the macroscopic loading parameter space $\mathfrak{T}$. Recall that $\boldsymbol{\xi}^q$ is an ordered list of the microscale deformation gradient, $\boldsymbol{F}$, for each finite element in the discretized microstructure (RUC). The error of the interpolated microscale field is evaluated by comparison with simulation data using Equations (21) and (20), respectively.

The homogenization error is shown in Figs. 11(a) and 11(b) for particle and matrix respectively. Fig. 11 shows that the homogenization error in $\boldsymbol{F}_m$ is higher (Fig. 11(b)), but only less than 13% of query points have a volume averaged error above 5% considering all modes. This is strong performance considering that no FEM analysis was performed, and the deformation gradient field (represented by $Ne = 486{,}051$ finite elements) is approximated using MNROM. On the other hand, some of the query points (less then 1.25%) have a homogenization error above 10%. These are usually query points close to the loading envelope or in a region where the manifold data density is substantially low.

To understand these errors, note that Isomap is not based on exact geodesics. Therefore, the reduced space $\mathcal{A}$ does not unfold the manifold $\mathcal{M}$ perfectly. This indicates that some degree of noise is involved in the data associated with $\mathcal{A}$. Since the accuracy of the computed geodesics directly depends on the density of data, the degree of noise indicates the amount of data sparsity. Insufficient data density also leads to inadequate NN learning [54,58] and deterioration of $\mathfrak{P}$ map. Future enhancements to the MNROM (e.g. pattern/physics based discretization) are needed to reduce this error. Nevertheless, these first results indicate the strong potential of this novel manifold-based reduced order method.

Minimum, maximum, mean and median of the volume averaged error over all query points for all modes are listed in Table 5. Note that the data reconstruction process is well preserved using MNROM with the mean error less than 3.5% (median error less than 2%) for all cases. Also, we note that among all modes, the homogenization error from 100 query points is higher for Mode 3. Therefore, we analyze the Mode 3 error in more depth.

The mean and standard deviation of the localization error defined in Equation (20) computed over the finite element field (i.e. deformation gradient) for 100 random query points from Mode 3 are shown in Figs. 12(a) and 12(b). Minimum, maximum, mean and median of the mean($\mathcal{E}_m$) error evaluated over the deformation gradient field for the population of 100 random query points from Mode 3 are listed in Table 6. Similar to the homogenization process (see Fig. 11), the localization error is of the same order. Moreover, since $^0\boldsymbol{F}$ is equal to $^0\boldsymbol{U}$ in our analysis, we can also get an estimate on the quality of the microscopic strain field from Fig. 12.

4.5. Homogenization of material response

To understand further the quality of MNROM solution, we are interested in predicting the homogenized strain energy density function (see Equation (6)). Fig. 13 shows the deviatoric (Fig. 13(a)) and volumetric (Fig. 13(b)) parts of the strain

Table 5
Quality of the MNROM for all modes computed from Equation (21) for 100 query points in each mode.

Loading cases		Min. [%]	Max. [%]	Mean [%]	Median [%]
Mode 1	Particle	0.0464	4.1540	0.2860	0.2469
	Matrix	0.2413	11.5384	2.2622	1.8902
Mode 2	Particle	0.0275	0.7621	0.1737	0.1235
	Matrix	0.3989	9.6881	2.5506	1.8707
Mode 3	Particle	0.0310	0.9997	0.2308	0.1274
	Matrix	0.4140	11.8873	3.3761	1.9683
Mode 4	Particle	0.0905	2.4268	0.3194	0.2869
	Matrix	0.6626	10.2583	2.2163	1.7815

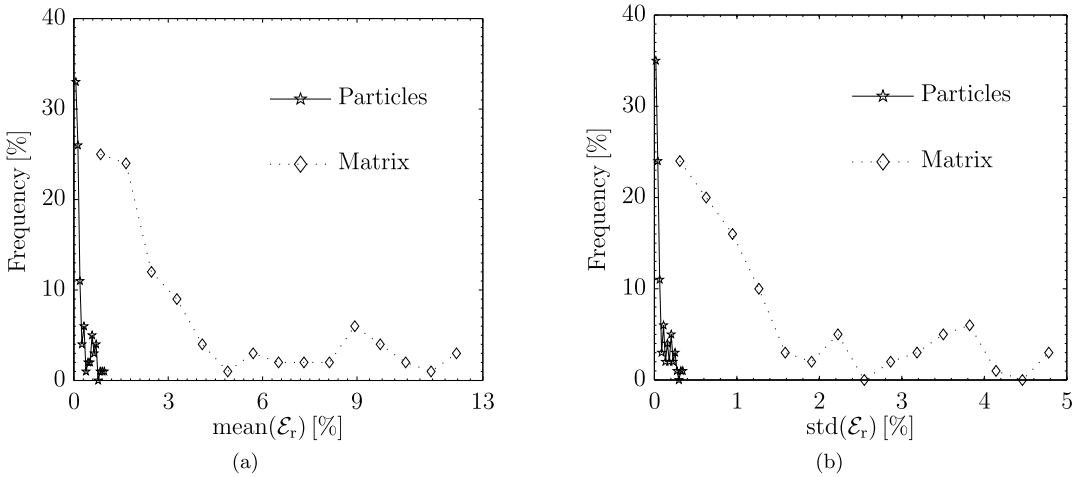

Fig. 12. Distribution of the local error (localization) given by Equation (20) for the 100 randomly selected query points from Mode 3. (a) Mean error and (b) standard deviation of the finite element field for 100 query points.

Table 6
Localization error characteristics of MNROM for mean($\mathcal{E}_m$) error from Equation (20) (see also Fig. 12(a)) of the deformation gradient field for population of 100 random query points from Mode 3.

Min.	Max.	Mean	Median
0.4519	12.5747	3.6266	2.1200

energy density function. The volumetric potential, ${}^0W_J(J)$, shows remarkable correlation between detailed parallel simulations using *PGFem3D* and MNROM (see Fig. 13(b)). A moderate error from MNROM is noticeable, especially for large volume changes ($J < 0.8$ and $J > 1.2$). The deviatoric potential, ${}^0W_C(\widehat{\mathbf{C}})$, comparison is more difficult to interpret since it depends on a second-order tensor. Therefore, we plot ${}^0W_C(\widehat{\mathbf{C}})$ as a function of $\|\widehat{\mathbf{C}}\|$ in Fig. 13(b). Furthermore, we carry out an error estimate for the homogenized potential energy. For that purpose, we define an error measure as

$$\mathcal{E}_{{}^0W} = \frac{\left|{}^0W^{ROM} - {}^0W^{FEM}\right|}{{}^0W^{FEM}} \times 100\,[\%]. \tag{22}$$

As observed in Fig. 13, the total potential energy, ${}^0W$, ranges from 0.05 MPa to 3 MPa. The median error ($\mathcal{E}_{{}^0W}$) is 10%, and 75% of the cases are below 20% error as computed from Equation (22). Moreover, points with high error ($> 20\%$) are concentrated in low to moderate potential energy regions. From Fig. 13 it can be seen that the volumetric energy is higher compared to the deviatoric one for large strains. Considering our mode construction (recall Table 2), we see that the principal stretches are either all positive or all negative in Modes 1 and 4, respectively. Therefore, the portions of high strain and potential energy are associated with Modes 1 and 4 (see Fig. 13(b)). Moreover, the points with increased errors are close to the loading envelope of Modes 1 and 4. Points with low to moderate potential energy and low volumetric deformation are mostly in Modes 2 and 3 (see Table 2), where the signs of the principal stretches are mixed. The data pattern for Modes 2 and 3 is quite complex, and data is sparse compared to Modes 1 and 4 (see target range in Table 4). Moreover, the degree of nonlinearity of Modes 2 and 3 is higher (see decay of residual variance in Fig. 6). Overall, the results suggest an acceptable agreement between detailed FEM simulations and MNROM. Once more, future enhancements

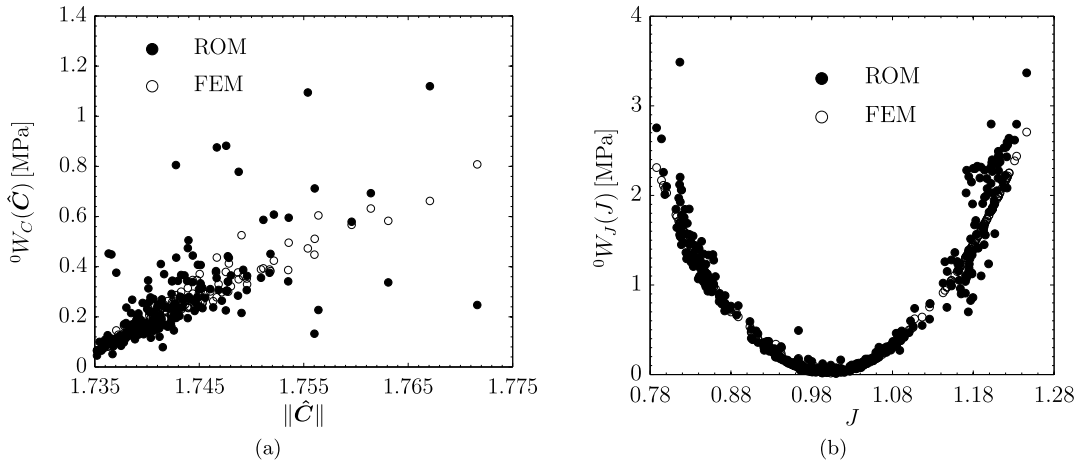

Fig. 13. Macroscale strain energy density function, MNROM versus FEM. (a) The deviatoric potential, $^0W_C(\widehat{\boldsymbol{C}})$. (b) The volumetric potential, $^0W_J(J)$.

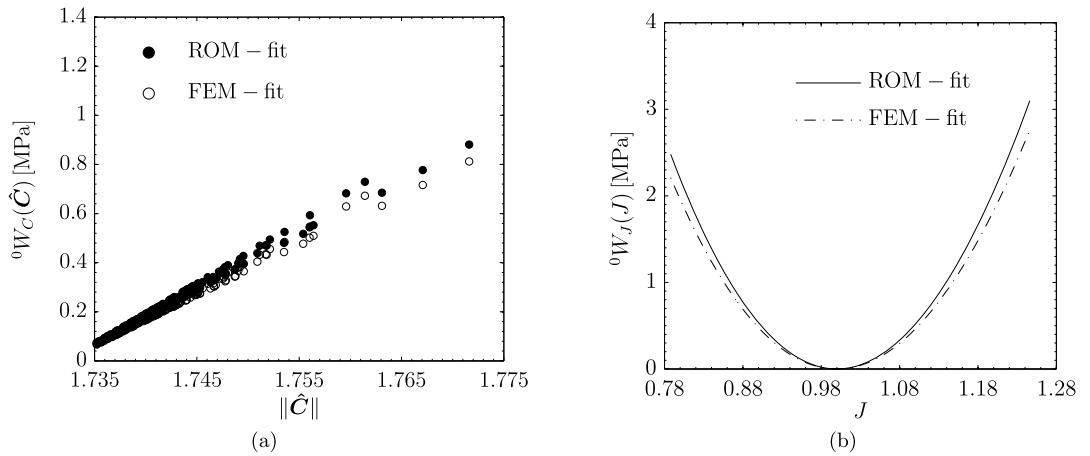

Fig. 14. Least-square fit of the macroscale strain energy density function, MNROM versus FEM. (a) The deviatoric potential, $^0W_C(\widehat{\boldsymbol{C}})$. (b) The volumetric potential, $^0W_J(J)$.

Table 7
Homogenized material properties.

Source	κ [MPa]	μ_{10} [MPa]	μ_{01} [MPa]
MNROM	105	13.45	13.45
FEM	94	12.40	12.40

to the MNROM including pattern/physics based discretization and enhancement or replacement of NN map with machine learning algorithms are needed to reduce this error. Nonetheless, Fig. 13 shows that the MNROM discovers with reasonable accuracy the homogenized constitutive laws for a large number of query points. Finally, we note that the functional form of these macroscale potentials is not assumed *a priori* and is discovered from our data without any additional large parallel simulations.

Since the spread in the data complicates the analysis (especially for the deviatoric portion of the potential function), we use model calibration to construct the homogenized potentials with volumetric and deviatoric split as $^0W(\boldsymbol{C}) = {}^0W_C(\widehat{\boldsymbol{C}}) + {}^0W_J(J)$. Although the functional form of the macro-potential can be obtained from results in Fig. 13, we use expressions of the micro-potential functions in Equation (18) for simplicity. Fig. 14 depicts model calibration using the volumetric (Fig. 14(b)) and deviatoric (Fig. 14(a)) functions (see Equation (18)) for both the FEM and MNROM data from Fig. 13. Both the FEM and MNROM parameterizations show excellent agreement for both the volumetric and the deviatoric potentials. Finally, the homogenized material constants for both FEM and MNROM models are listed in Table 7.

We also investigate the macroscopic first Piola stress tensor, $^0\boldsymbol{P}$, and compare it to the FEM solution. Since $^0\boldsymbol{F}$ is the energy conjugate to $^0\boldsymbol{P}$, in Fig. 15(a), we plot the Frobenius norm of $^0\boldsymbol{P}$ with corresponding Frobenius norm of $^0\boldsymbol{F}$ for all four modes. We can see that the points corresponding to $\|^0\boldsymbol{P}\|$ computed by MNROM are clustered around the points which

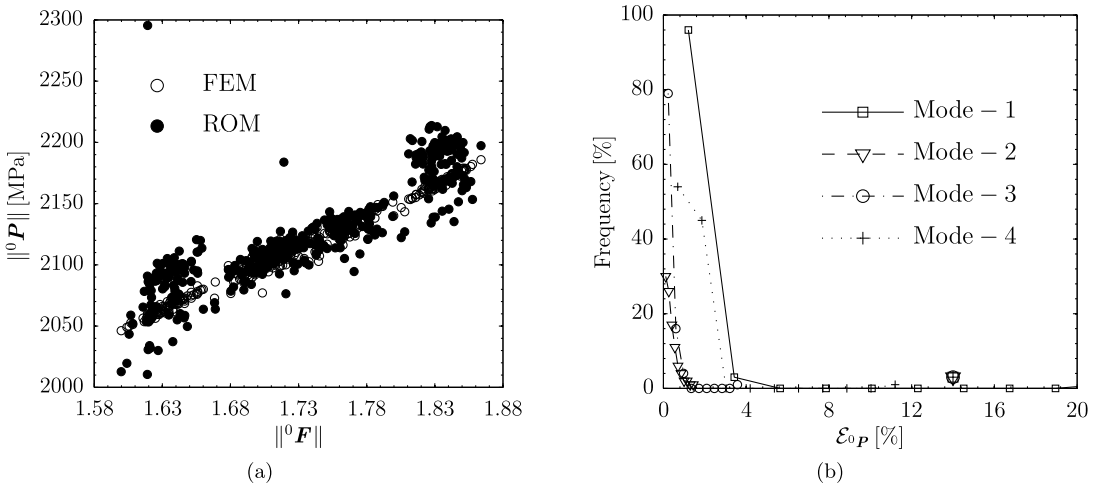

Fig. 15. Macroscale first Piola stress tensor, ${}^0\boldsymbol{P}$, MNROM versus FEM. (a) Frobenius norm of ${}^0\boldsymbol{P}$ against Frobenius norm of ${}^0\boldsymbol{F}$. (b) Distribution of the homogenization error given by Eq. (23).

are calculated by the FEM. However, it is not easy to interpret a second-order tensor from its norm alone. Therefore, we compute the error as given in Equation (23) to understand accuracy of the method. The error plot is shown in Fig. 15(b), where 99.5% of the query points have less than $\mathcal{E}_{^0\boldsymbol{P}} = 5\%$ error, and 67.25% of all query points have less than 1% error for all modes.

$$\mathcal{E}_{^0\boldsymbol{P}} = \frac{\|^0\boldsymbol{P}^{ROM} - {}^0\boldsymbol{P}^{FEM}\|}{\|^0\boldsymbol{P}^{FEM}\|} \times 100\,[\%]. \tag{23}$$

Although some query points show moderate error for the energy density function (see Fig. 13) and stress (see Fig. 15(a)) as compared to FEM, we note that this is only for a small portion of the query points. Moreover, the pattern/physics based discretization technique will help to reduce such errors as mentioned before. In terms of coupled multiscale analysis, these errors will not have any effect when MNROM is used as an accelerator in two-scale (structure) calculations. Moreover, one can use the calibrated multiscale potentials (see Fig. 14) at the macroscale.

4.6. Localization of material response

In the previous section, we have investigated homogenization properties of MNROM. Now, we are interested in the localization accuracy of MNROM and its ability to predict the local (element-wise) engineering fields derived from $\boldsymbol{F}$. Therefore, we introduce the Almansi strain, $\boldsymbol{e}$, defined as

$$\boldsymbol{e} = \frac{1}{2}(\boldsymbol{1} - \boldsymbol{F}^{-1}\boldsymbol{F}^{-T}). \tag{24}$$

To quantify the strain error between the FEM and MNROM solutions at each local point $\boldsymbol{Y}$ in the microstructure (i.e. each finite element in RUC), we introduce the effective strain error:

$$\mathcal{E}_e = \frac{|\|\boldsymbol{e}^{ROM}\|_{\mathcal{F}} - \|\boldsymbol{e}^{FEM}\|_{\mathcal{F}}|}{\|\boldsymbol{e}^{FEM}\|_{\mathcal{F}}} \times 100\,[\%]. \tag{25}$$

In order to understand representative loading conditions, we investigate a query point from Mode 3 with the homogenization error of ${}^0\mathcal{E}_p = 0.3316\%$, and ${}^0\mathcal{E}_m = 4.9335\%$ as computed from Equation (21). Looking at Fig. 11 (also see Table 5) and quantifying the percentage, the solution quality of 87.75% of the query points is better than this selected point while considering all modes. Therefore, this selection is representative of a large range of different loading conditions (i.e. not present in the original dataset).

To get a clear understanding about both the magnitude of field and distributions of error with respect to the local deformation extent within each finite element, we plot two joint probability distributions. Fig. 16(a) shows the joint probability distribution of $\mathcal{E}_m$ in Equation (20) and $\|\boldsymbol{F}^{FEM}\|_{\mathcal{F}}$, and Fig. 16(b) displays the joint probability distribution of $\mathcal{E}_e$ in Equation (25) and $\|\boldsymbol{e}^{FEM}\|_{\mathcal{F}}$. Here we view $\|\boldsymbol{e}\|_{\mathcal{F}}$ like the microscopic effective Almansi strain. Since particles behave as rigid-like, deformation in particles is negligible, and we focus on the matrix. The joint probability distribution is constructed from a cloud of points representing individual finite elements within the matrix phase (285,380 elements in the matrix).

Fig. 16(a) shows that most finite elements in the matrix carry a mean localization error of 5.3786% for this loading case (compare also to Fig. 12), and that the deformation is concentrated between $\|\boldsymbol{F}^{FEM}\|_{\mathcal{F}} = 1.58$ and $\|\boldsymbol{F}^{FEM}\|_{\mathcal{F}} = 1.75$ (note that $\|\boldsymbol{1}\|_{\mathcal{F}} = \sqrt{3} = 1.732$). Moreover, Fig. 16(a) shows that the error $\mathcal{E}_m$ is concentrated between ∼4–7% and decays quickly.

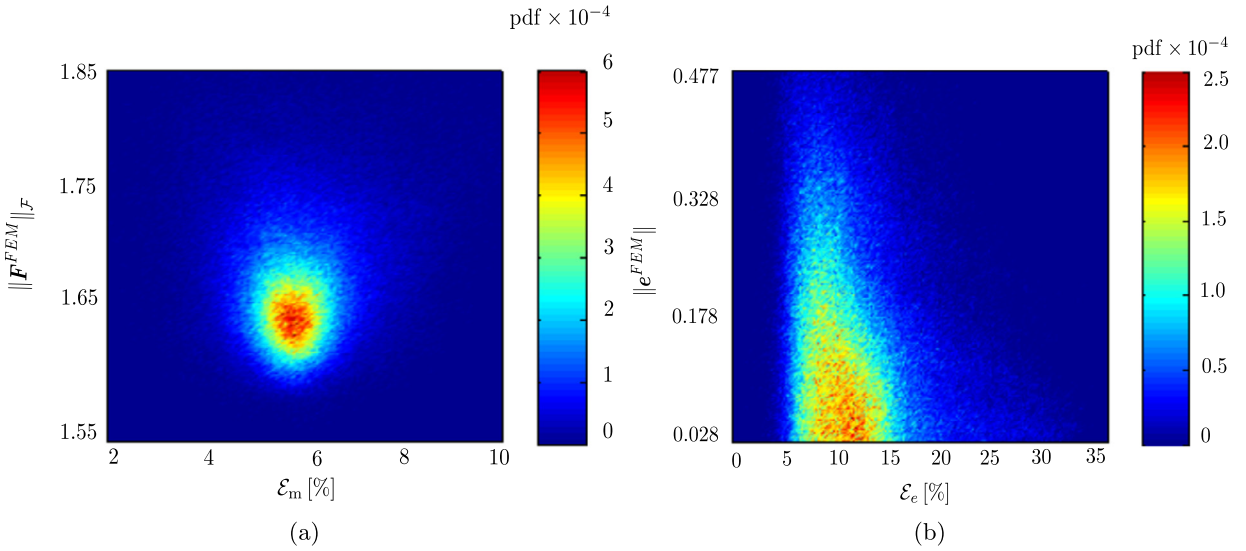

Fig. 16. Joint probability distribution (computed in discrete element-wise sense) of the local fields (in matrix phase). (a) $\mathcal{E}_m$ and $\|\boldsymbol{F}^{FEM}\|_{\mathcal{F}}$. (b) $\mathcal{E}_e$ and $\|\boldsymbol{e}^{FEM}\|_{\mathcal{F}}$.

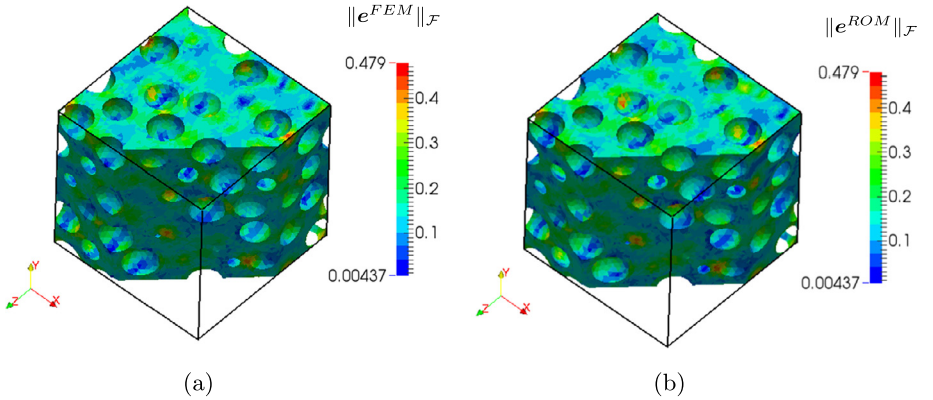

Fig. 17. Visualization of the microscopic effective Almansi strain ($\|\boldsymbol{e}\|_{\mathcal{F}}$) for $\boldsymbol{\eta}^q = \{{}^0\lambda_1 = 0.9762,\ {}^0\lambda_2 = 0.9181,\ {}^0\lambda_3 = 1.0274,\ \varphi^1 = 4.03$ [rad], $\varphi^2 = 0.0322$ [rad], $\varphi^3 = 1.3527$ [rad]$\}$ (note, particles are rigid-like and hence are removed for the visualization purpose). (a) FEM simulation. (b) MNROM analysis.

Fig. 16(b) reveals that the mean microscopic effective Almansi strain error calculated at every finite element in the matrix is 13.6321%. Note that the regions of high strains are concentrated between errors of 5–15%. Moreover, 50% of the finite elements have errors below 10% (median error is 9.9678%), and 78% of finite elements in the matrix have errors below 20%. Finally, we can see that the largest errors are at small to moderate strains. This is not surprising since the Almansi strain is derived from $\boldsymbol{F}$ (see Equation (24)), and any small noise near the unloaded state ($\boldsymbol{F} = \boldsymbol{1}$) is contributing to this relative error measure. These results show good localization characteristics of the MNROM for both $\boldsymbol{F}$ as well as engineering measures, such as the microscopic effective Almansi strain (defined as $\|\boldsymbol{e}\|_{\mathcal{F}}$ in this work).

Fig. 17 compares the microscopic effective Almansi strain within the matrix for both the FEM (left) and MNROM (right) analysis. As can be seen, the MNROM captures well highly localized strain regions (see top cell surface and cut vertical surface) as well as the overall strain distribution (see the rest of the cell). Once more, we remark that no additional HPC simulations were performed for the case computed from the MNROM.

5. Conclusion

We have proposed here a novel manifold-based reduced order model for multiscale modeling of nonlinear hyperelastic materials in finite strain setting. The reduced order model is built on top of Isomap, which provides dimensionality reduction from the high-dimensional data stemming from large parallel computational homogenization simulations. The map between the set of macroscopic loading parameters and the reduced space is accomplished by the Neural Network. Once

constructed, the manifold-based reduced order model provides both homogenization and localization of the multiscale solution for complex three-dimensional material domains. Thus, solution of the large microscale boundary value problem to arbitrary multiscale loading conditions is approximated quickly without the need for additional large parallel finite element simulations.

In order to build the manifold, we employ the large parallel three-dimensional finite strains solver, *PGFem*3*D*, and perform several parallel simulations using a statistically representative unit cell. This statistically representative unit cell is generated by a packing algorithm. The multiscale loading conditions are simulated in terms of the macroscopic principal stretches as well as the orthogonal principal directions. Therefore, arbitrary multiscale loading conditions can be applied. In order to obtain a uniform discretization for rotational parameters, we employ the HEALPix grid. The manifold-based reduced order model is verified step by step using traditional machine-learning procedures. Next, we perform homogenization and localization of the multiscale solution for data points not in the digital database. Rigorous assessment of both homogenization and localization errors is performed. We show that the manifold-based reduced order model discovers the homogenized material response as well as provides microscopic fields of interest. In this work, we select the deformation gradient as the building block of the manifold, since the other physical fields (i.e. Almansi strain, Piola–Kirchhoff stress) can be easily derived.

The proposed manifold-based reduced order model can be used for material classification and lends itself to predictive scientific studies as well as Virtual Materials Testing. It can also be used to accelerate fully coupled multiscale computational homogenization simulations (i.e. FE^2). Future studies on pattern/physics based discretization are needed to improve this reduced order model. Moreover, the manifold-based reduced order model for problems with both geometric and material nonlinearities (e.g. plasticity, damage) is a natural next step.

Acknowledgements

This work was supported by the Multiscale Design Systems, LLC under the contract No. FA8651-14-C-0045 (Eglin Air Force Base, STTR Phase II project) funded by the Department of Defense, and by the Department of Energy, National Nuclear Security Administration, under the award No. DE-NA0002377 as part of the Predictive Science Academic Alliance Program II.

References

[1] R.W. Ogden, D.G. Roxburgh, A pseudo-elastic model for the Mullins effect in filled rubber, Proc. R. Soc. Lond., Ser. A 455 (1999) 2861–2877.
[2] J.S. Bergström, M.C. Boyce, Constitutive modeling of the large strain time-dependent behavior of elastomers, J. Mech. Phys. Solids 46 (1998) 931–954.
[3] K. Millera, K. Chinzeib, Mechanical properties of brain tissue in tension, J. Biomech. 35 (2002) 483–490.
[4] M.H. Holmes', V.C. Mow, The nonlinear characteristics of soft gels and hydrated connective tissues in ultrafiltration, J. Biomech. 23 (1990) 1145–1156.
[5] S.R. Swanson, L.W. Christensen, A constitutive formulation for high-elongation propellants, J. Spacecr. Rockets 20 (1983) 559–566.
[6] M.R. Baer, Modeling heterogeneous energetic materials at the mesoscale, Thermochim. Acta 384 (2002) 351–367.
[7] E. Weinan, Principles of Multiscale Modeling, Cambridge University Press, Cambridge, UK, 2011.
[8] J. Fish, Practical Multiscaling, John Wiley & Sons, New York City, NY, 2013.
[9] R. Hill, On constitutive macro-variables for heterogeneous solids at finite strain, Proc. R. Soc. Lond., Ser. A 326 (51) (1972) 245–271.
[10] M.G.D. Geers, V. Kouznetsova, W.A.M. Brekelmans, Multi-scale computational homogenization: trends and challenges, J. Comput. Appl. Math. 234 (2010) 2175–2182.
[11] C. Miehe, Computational micro-to-macro transitions for discretized micro-structures of heterogeneous materials at finite strains based on the minimization of averaged incremental energy, Comput. Methods Appl. Mech. Eng. 192 (2003) 559–591.
[12] T.I. Zohdi, J.T. Oden, G.J. Rodin, Hierarchical modeling of heterogeneous bodies, Comput. Methods Appl. Mech. Eng. 138 (1996) 273–298.
[13] K. Matouš, P.H. Geubelle, Multiscale modelling of particle debonding in reinforced elastomers subjected to finite deformations, Int. J. Numer. Methods Eng. 65 (2006) 190–223.
[14] Z.F. Khisaeva, M. Ostoja-Starzewski, On the size of RVE in finite elasticity of random composites, J. Elast. 85 (2006) 153–173.
[15] J. Fish, K. Shek, Multiscale analysis of composite materials and structures, Compos. Sci. Technol. 60 (2000) 2547–2556.
[16] M. Mosby, K. Matouš, Hierarchically parallel coupled finite strain multiscale solver for modeling heterogeneous layers, Int. J. Numer. Methods Eng. 102 (2015) 748–765.
[17] V.P. Nguyen, M. Stroeven, L.J. Sluys, Multiscale continuous and discontinuous modeling of heterogeneous materials: a review on recent development, J. Multiscale Model. 3 (2011) 229–270.
[18] F. Feyel, J.L. Chaboche, FE^2 multiscale approach for modelling the elasto-viscoplastic behaviour of long fibre SiC/Ti composite materials, Comput. Methods Appl. Mech. Eng. 183 (2000) 309–330.
[19] M. Mosby, K. Matous, Computational homogenization at extreme scales, Extreme Mech. Lett. 6 (2016) 68–74.
[20] J. Yvonnet, Q.-C. He, The reduced model multiscale method (R3M) for the non-linear homogenization of hyperelastic media at finite strains, J. Comput. Phys. 223 (2007) 341–368.
[21] J.A. Hernández, J. Oliver, A.E. Huespe, M.A. Caicedo, J.C. Cante, High-performance model reduction techniques in computational multiscale homogenization, Comput. Methods Appl. Mech. Eng. 276 (2014) 149–189.
[22] F. El Halabi, D. González, A. Chico, M. Doblaré, FE^2 multiscale in linear elasticity based on parametrized microscale models using proper generalized decomposition, Comput. Methods Appl. Mech. Eng. 257 (2013) 183–202.
[23] C. Oskay, J. Fish, Eigendeformation-based reduced order homogenization for failure analysis of heterogeneous materials, Comput. Methods Appl. Mech. Eng. 196 (2007) 1216–1243.
[24] B. Ganapathysubramanian, N. Zabaras, A non-linear dimension reduction methodology for generating data-driven stochastic input models, J. Comput. Phys. 227 (2008) 6612–6637.
[25] P. Kerfriden, J.-J. Ródenas, S.P.-A Bordas, Certification of projection-based reduced order modelling in computational homogenisation by the constitutive relation error, Int. J. Numer. Methods Eng. 97 (2014) 395–422.
[26] A. Chatterjee, An introduction to the proper orthogonal decomposition, Curr. Sci. 78 (2000) 808–817.

[27] G. Berkooz, P. Holmes, J.L. Lumley, The proper orthogonal decomposition in the analysis of turbulent flows, Annu. Rev. Fluid Mech. 25 (1) (1993) 539–575.
[28] J. Yvonnet, E. Monteiro, Q.-C. He, Computational homogenization method and reduced database model for hyperelastic heterogeneous structures, Int. J. Multiscale Comput. Eng. 11 (2013) 201–225.
[29] I. Temizer, P. Wriggers, An adaptive method for homogenization in orthotropic nonlinear elasticity, Comput. Methods Appl. Mech. Eng. 196 (2007) 3409–3423.
[30] I. Temizer, T.I. Zohdi, A numerical method for homogenization in non-linear elasticity, Comput. Mech. 40 (2007) 281–298.
[31] J. Ghaboussi, J.H. Garret Jr., X. Wu, Knowledge-based modeling of material behavior with neural networks, J. Eng. Mech. 117 (1991) 132–153.
[32] J.F. Unger, C. Könke, Coupling of scales in multiscale simulation using neural network, Comput. Struct. 86 (2008) 1994–2003.
[33] B.A. Le, J. Yvonnet, Q-C. He, Computational homogenization of nonlinear elastic materials using neural networks, Int. J. Numer. Methods Eng. (2015), http://dx.doi.org/10.1002/nme.4953.
[34] A.A. Shah, A survey of data-driven emulators for high dimensional spatia-temporal data, in: Proceedings of International Conference on Information Technology and Computer Science, ISBN 9788193137307, 2015.
[35] J.E. Andrade, X. Tu, Multiscale framework for behavior prediction in granular media, Mech. Mater. 41 (2009) 652–669.
[36] G.J. Dvorak, Transformation field analysis of inelastic composite materials, Proc. R. Soc. Lond. A 437 (1992) 311–327.
[37] R. Largenton, J.-C. Michel, P. Suquet, Extension of the nonuniform transformation field analysis to linear viscoelastic composites in the presence of aging and swelling, Mech. Mater. 73 (2014) 76–100.
[38] F. Fritzen, M. Leuschner, Reduced basis hybrid computational homogenization based on a mixed incremental formulation, Comput. Methods Appl. Mech. Eng. 260 (2013) 143–154.
[39] B. Klusemann, M. Ortiz, Acceleration of material-dominated calculations via phase-space simplicial subdivision and interpolation, Numer. Methods Eng. 103 (2015) 256–274.
[40] W. Xing, A.A. Shah, P.B. Nair, Reduced dimensional Gaussian process emulators of parametrized partial differential equations based on isomap, Proc. R. Soc. Lond. A 471 (2174) (2015) 20140697.
[41] J.B. Tenenbaum, V. De Silva, J.C. Langford, A global geometric framework for nonlinear dimensionality reduction, Science 290 (2000) 2323–2326.
[42] C.-G. Li, J. Guo, G. Chen, X.-F. Nie, Z. Yang, A version of isomap with explicit mapping, Proceedings of the Fifth International Conference on Machine Learning and Cybernetics, Dalian, 13–16 August 2006.
[43] M. Belkin, P. Niyogi, Laplacian eigenmaps for dimensionality reduction and data representation, Neural Comput. 15 (2003) 1373–1396.
[44] S.T. Roweis, L.K. Saul, Nonlinear dimensionality reduction by locally linear embedding, Science 290 (2000) 2323–2326.
[45] A.T.H. Lee, M. Brandyberry, K. Matouš, Three-dimensional reconstruction of statistically optimal unit cells of polydisperse particulate composites from microtomography, Phys. Rev. E 80 (2009) 061301.
[46] S. Torquato, Random Heterogeneous Materials, Springer, New York, USA, 2002.
[47] M. Mosby, K. Matouš, On mechanics and material length scales of failure in heterogeneous interfaces using a finite strain high performance solver, Model. Simul. Mater. Sci. Eng. 23 (8) (2015) 085014.
[48] K.M. Gorski, E. Hivon, A.J. Banday, B.D. Wandelt, F.K. Hansen, M. Reinecke, M. Bartelmann, Healpix: a framework for high-resolution discretization and fast analysis of data distributed on the sphere, Astrophys. J. 622 (2005) 759–771.
[49] V.D. Silva, J.B. Tenenbaum, Global versus local methods in nonlinear dimensionality reduction, Adv. Neural Inf. Process. Syst. (2002) 705–712.
[50] V.D. Maaten, J.P. Laurens, E.O. Postma, H.J. van den Herik, Dimensionality reduction: a comparative review, J. Mach. Learn. Res. 10 (1–41) (2009) 66–71.
[51] B. Schölkopf, A. Smola, K.R. Müller, Kernel principal component analysis, in: Artificial Neural Networks — ICANN'97, 1997, pp. 583–588.
[52] R.R. Coifman, S. Lafon, Diffusion maps, Appl. Comput. Harmon. Anal. 21 (1) (2006) 5–30.
[53] M.H. Beale, M.T. Hagan, H.B. Demuth, Neural Network Toolbox™, User's Guide, The MathWorks, Inc., Natick, MA, USA, 1992–2015.
[54] V. Tresp, S. Ahmad, R. Neuneier, Training neural networks with deficient data, Adv. Neural Inf. Process. Syst. (1994) 128.
[55] K. Hornik, M. Stinchcombe, H. White, Multilayer feedforward networks are universal approximators, Neural Netw. 2 (1989) 359–366.
[56] B.G. Sumpter, C. Getino, D.W. Noid, Theory and applications of neural computing in chemical science, Annu. Rev. Phys. Chem. 45 (1994) 439–481.
[57] W.L. Buntine, A.S. Weigend, Baysian back-propagation, Complex Syst. 5 (1991) 603–643.
[58] C. Cortes, L.D. Jackel, W.-P. Chiang, Limits on learning machine accuracy imposed by data quality, in: In, AAAI Press, 1995, pp. 57–62.
[59] K.R. Srinivasan, K. Matouš, P.H. Geubelle, Generalized finite element method for modeling nearly incompressible bimaterial hyperelastic solids, Comput. Methods Appl. Mech. Eng. 197 (51) (2008) 4882–4893.
[60] K. Matouš, P.H. Geubelle, Finite element formulation for modeling particle debonding in reinforced elastomers subjected to finite deformations, Comput. Methods Appl. Mech. Eng. 196 (1) (2006) 620–633.
[61] J.R. Munkres, Topology, 2nd edn., Prentice Hall, NJ, USA, 2000.
[62] M. Sniedovich, Dijkstra's algorithm revisited: the dynamic programming connexion, Control Cybern. 35 (3) (2006) 599.
[63] M. Bernstein, V.D. Silva, J.C. Langford, J.B. Tenenbaum, Graph approximations to geodesics on embedded manifolds, Technical report, Stanford University, Stanford, December 2000.
[64] J. Costa, A.O. Hero, et al., Geodesic entropic graphs for dimension and entropy estimation in manifold learning, IEEE Trans. Signal Process. 52 (8) (2004) 2210–2221.
[65] R.W. Floyd, Algorithm 113: treesort, Commun. ACM 5 (8) (1962) 434.
[66] H. Wendland, Scattered Data Approximation, Cambridge University Press, 2004.
[67] L. Györfi, M. Kohler, A. Krzyzak, H. Walk, A Distribution-Free Theory of Nonparametric Regression, Springer Science & Business Media, New York, Berlin, Paris, 2006.
[68] E.A. Nadaraya, On estimating regression, Theory Probab. Appl. 9 (1963) 141–142.
[69] C.E. Rasmussen, C.K.I. Williams, Gaussian Processes for Machine Learning, The MIT Press, Cambridge, Massachusetts, USA, 2006.
[70] M. Debruynei, M. Hubert, J.A. Suykens, Model selection in kernel based regression using the influence function, J. Mach. Learn. Res. 9 (2008) 2377–2400.
[71] F. Liang, K. Mao, M. Liao, S. Mukherjee, M. West, Nonparametric Bayesian kernel models, Department of Statistical Science, Duke University, 2007, Discussion Paper 07–10.
[72] D.S. Stafford, T.L. Jackson, Using level sets for creating virtual random packs of non-spherical convex shapes, J. Comput. Phys. 229 (2010) 3295–3315.
[73] J.C. Michel, O. Lopez-Pamies, P.P. Castañeda, N. Triantafyllidis, Microscopic and macroscopic instabilities in finitely strained porous elastomers, J. Mech. Phys. Solids 55 (5) (2007) 900–938.
[74] P. Wriggers, J.C. Simo, A general procedure for the direct computation of turning and bifurcation points, Int. J. Numer. Methods Eng. 30 (1) (1990) 155–176.